NATIONAL ENERGY TECHNOLOGY LABORATORY

Experimental investigation on the binary/ternary fluidization behavior of Geldart D type spherical LDPE, Geldart D type cylindrical wood and Geldart B type sand particles

March 2021

U.S. DEPARTMENT OF ENERGY | NATIONAL ENERGY TECHNOLOGY LABORATORY

Office of Fossil Energy

NETL-TRS-2725-2021

Disclaimer

This project was funded by the United States Department of Energy, National Energy Technology Laboratory, in part, through a site support contract.

Suggested Citation: Li, C., Gao, X., Rowan, S., Hughes, B., Jeremy S. Harris, and Rogers, W. A. Experimental investigation on the binary/ternary fluidization behavior of Geldart D type spherical LDPE, Geldart D type cylindrical wood and Geldart B type sand particles; NETL-TRS-2725-2021; NETL Technical Report Series; U.S. Department of Energy, National Energy Technology Laboratory: Morgantown, WV, 2021. DOI 10.2172/1776642.

An electronic version of this report can be found at: https://netl.doe.gov/TRS

Experimental investigation on the binary/ternary fluidization behavior of Geldart D type spherical LDPE, Geldart D type cylindrical wood, and Geldart B type sand particles

Cheng Li[1, 3], Xi Gao[1, 2], Steven L. Rowan[1,2], Bryan Hughes[1,2], Jeremy S. Harris[4], William A. Rogers[1]

[1] National Energy Technology Laboratory,
3610 Collins Ferry Road, Morgantown, WV 26507

[2] NETL Support Contractor,
3610 Collins Ferry Road, Morgantown, WV 26507

[3] Oak Ridge Institute for Science and Education,
3610 Collins Ferry Road, Morgantown, WV 26507

[4]Attain, LLC
1600 Tysons Boulevard, Suite 1400, McLean, Virginia 22102

NETL-TRS-2725-2021

March 2021

NETL Contacts:

William A. Rogers, Principal Investigator

Jonathan Lekse, Technical Portfolio Lead

Bryan Morreale, Executive Director, Research & Innovation Center

This page intentionally left blank

Table of Contents

List of Figures

List of Tables

Acknowledgments

This work was performed in support of the U.S. Department of Energy's (DOE) Fossil Energy Crosscutting Technology Research Program. The research was executed through the National Energy Technology Laboratory's (NETL) Research and Innovation Center's Advanced Reaction Systems Field Work Proposal. This research was also supported in part by an appointment to the U.S. Department of Energy (DOE) Postgraduate Research Program at the National Energy Technology Laboratory (NETL) administered by the Oak Ridge Institute for Science and Education (ORISE).

The authors also wish to acknowledge technical assistance from Timothy Floyd and Bryan Hughes for their support in designing the experimental apparatus used in the detailed experiments.

EXECUTIVE SUMMARY

The series of experiments have been performed on a 2.5-inch cylindrical bed made of acrylic with full optical access and multiple pressure ports at various heights of the bed.

The material of interest includes in the investigation include Geldart type D cylindrical hardwood pellets, Geldart type D spherical LDPE, and Geldart type B sand particles. The wood particles have a diameter of around 6.6 mm and a length of 13.2 mm, corresponding to an aspect ratio of 1:2. The spherical LDPE particles and the sand particles have a Sauter Mean Diameter of 3.75 mm, and 0.5 mm, respectively. The experiment series involved the fluidization of the above-mentioned single particle type, as well as the fluidization of binary and ternary mixtures with varying superficial velocities. Following six types of experiments have been completed:

(a) Geldart type D spherical LDPE particles
(b) Geldart type B sand particles
(c) Geldart type D cylindrical hardwood pellets
(d) LDPE and hardwood pellets co-fluidization
(e) Sand and hardwood pellets co-fluidization
(f) Sand, LDPE, and hardwood pellets co-fluidization

For experiment (a) – (c), the aim is to provide standard fluidization tests of these materials in the bed, providing minimum fluidization velocity (U_{mf}) values for planning on the experiment (d) – (f). For experiment (d) - (f), the superficial gas velocities were scaled on the U_{mf} of LDPE, sand, and sand, respectively. The initial static bed heights were based on the bed height of LDPE, sand, and sand/LDPE mixture. In general, the tested superficial velocities have been varied from 1.5 U_{mf} to 3.7 U_{mf}, 1.5 U_{mf} to 5.0 U_{mf}, and 1.5 U_{mf} – 4.0 U_{mf}, respectively. The steady-state data have been acquired for all cases, and the transient mixing data have been recorded for sand/wood, and LDPE/wood binary mixing, and sand/LDPE/wood ternary mixing, all at 3 U_{mf}. The static bed height has been tested at both 7.62 cm and 15.24 cm for the binary mixing case and only at 7.62 cm for the ternary mixing. The fraction of the hardwood particle components has been varied by count from 50 – 200 for all cases. The reported results include:

(a) high-speed visualization of the fluidization processes;
(b) high-speed differential pressure and bed height statistics;
(c) particle scale information includes particle velocity and orientation.

The objective of the current study is to provide a series of comprehensive fundamental investigation on the fluidization, and mixing/segregation behavior of plastic-biomass-sand mixtures. Furthermore, the obtained experimental data will be utilized to validate the computational models, specifically the non-spherical DEM solver that is being developed in NETL. Non-spherical shaped particles are commonly seen in nature and widely used in industrial applications. However, the influence of model parameters on quantities of interest as well as their sensitivities with varying particle characteristics and flow conditions remain to be elucidated. A high-quality validation is henceforth critical to assess the predictability of such modeling techniques.

1. INTRODUCTION

Fluidized beds have been widely used in industrial applications owing to the high efficiencies in heat transfer, uniform and controllable temperatures, favorable gas–solid contacting and the ability to handle a wide variation in particulate properties (Cocco et al. 2014).

Recently, the application of biomass and plastic particles in fluidized bed systems has become increasingly popular and is investigated in many studies(Cui & Grace 2007; Pinto et al. 2003; Xue et al. 2015). The advantages of the application of biomass and plastic particles include (1) abundant supply of the raw material, and (2) great potential for sustainable energy conversion processes such as combustion, gasification, and pyrolysis, to reduce greenhouse gas emissions. For example, the US produces approximately 292.4 million tons of municipal solid waste (MSW) in the year 2018, and the number is still increasing at an average rate of 5.2 million tons per year(US Environmental Protection Agency 2020). Among that, plastic and wood constitute 53.8 million tons, however, 67% of waste wood and 75% of waste plastic end up in landfill sites causing great land resources waste, and various environmental problems. Better utilization of these waste plastic and wood will help mitigate the adverse effects they generate on the environment and establish sustainable energy conversion processes to reduce carbon emissions.

However, biomass particles are usually of non-spherical shape and large size making them more difficult to fluidize. Nevertheless, co-fluidization/co-pyrolysis of biomass and plastics have already been examined extensively (Abnisa & Wan Daud 2014; Costa et al. 2014; Martínez et al. 2014). Most of these studies are focused on batch reactors or fixed bed reactors, the slow pyrolysis processes and low-velocity fluidized bed. The inherent particle mixing is limited or slow. Relatively few studies have dedicated to characterizing biomass and plastic particles hydrodynamics and mixing in the fluidized bed under extended flow regimes or attempt to propose methods to enhance the mixing. Thus, further research is needed to provide baseline data on the fluidization and mixing of these particles and understand the underlying physics in the interactions between particles. To this end, this study aims to provide systematic hydrodynamics datasets for various particle systems that involve biomass and/or plastic particles.

In section 2, the experiment setup, material characteristics, experimental parameter space, along with the methodology of the machine learning-enabled image processing methods are presented. In section 3, the effects of cylindrical particle mass fraction, fluidization velocity, and static bed height on the cylinder dynamics and fluidization behavior were presented. Finally, the conclusions are presented in section 4.

2. METHODS

2.1 PARTICLE CHARACTERIZATION

The material of interest includes in the investigation include Geldart type D cylindrical hardwood pellets, Geldart type D spherical LDPE, and Geldart type B sand particles. Sample micrographs for both raw wood pellets and LDPE particles are provided in Figure 2-1. The particle characterization mainly employs the procedures established in the NETL's Multiphase Flow Analysis Laboratory (MFAL) (Tucker et al. 2013). The LDPE and sand particles used in the experiments are characterized using QICPIC (manufactured by Sympatec GmBH) providing both size and shape quantification of the particles, whereas the size of the wood pellets is too large for such analysis. As a result, the particles are imaged using a digital camera for size characterization.

The resultant volumetric particle size distribution including the cumulative distribution (Q3) and distribution density (q3) is provided in Figure 2-2 for both sand and LDPE particles. The integral particle information has been summarized in Table 2-1, including d_{50}, volumetric mean diameter (VMD), Sauter mean diameter (SMD), and sphericity. The sampled particles numbers are over 10^6 for both cases. To minimize the complications for non-spherical wood particles simulations validation effort, the raw cylindrical hardwood pellets are cut into equal length, resulting in monodispersed wood pellets for all current experiments. The final prepared cylindrical wood particles have a diameter of around 6.18 mm and a length of 12.36 mm, corresponding to an aspect ratio of 1:2. The spherical LDPE particles and the sand particles have a Sauter Mean Diameter of 3.75 mm, and 0.5 mm, respectively. Figure 2-3 displays the location of three types of particles according to the Geldart chart (Geldart 1973).

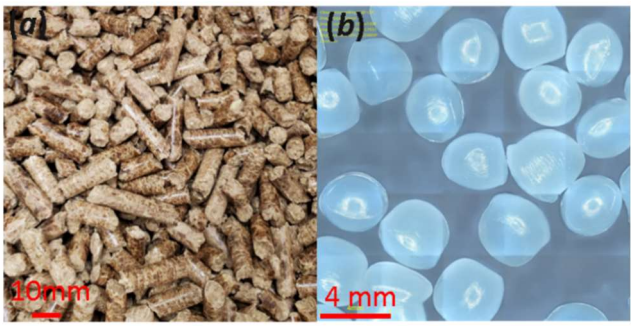

Figure 2-1: Micrographs of (a) raw cylindrical hardwood pellets, and (b) spherical LDPE particles

Table 2-1: Integral particles properties.

	LDPE	Sand	Wood
Particle Density/ $g \cdot cm^{-3}$	0.931	2.585	1.158
d_{50}/μm	3740.36	546.11	-
SMD/μm	3754.82	499.99	7920
VMD/μm	3785.31	551.93	9519
Sphericity/-	0.929±0.023	0.810±0.082	0.832
Particle number sampled/-	1365254	1107105	-

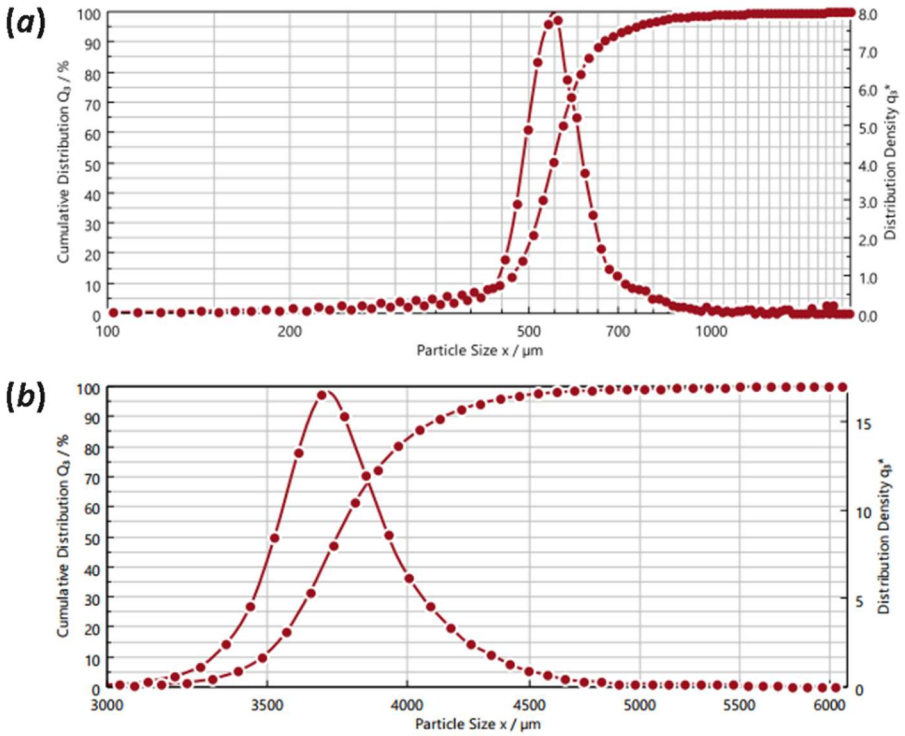

Figure 2-2: Particle size distribution of (a) sand particles, and (b) spherical LDPE particles

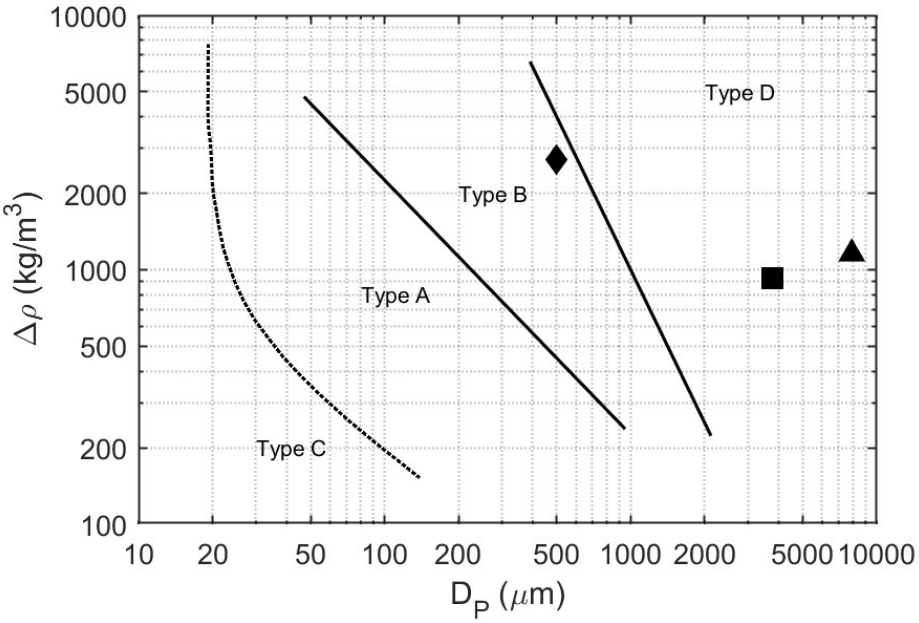

Figure 2-3: Geldart chart showing the location of sand (diamond), LDPE(triangle) and wood (square) particles used in the experiments.

2.2 MINIMUM FLUIDIZATION TESTS

Minimum fluidization velocity, U_{mf} corresponds to the superficial gas velocity at which the bed changes from a packed state to a fluidized state, and satisfying the condition that the drag force applied by the upward moving gas equals the weight of all the particles in bed(Kunii & Levenspiel 1991). The minimum fluidization test involves the recording of pressure drop over the entire bed at various flow rates, curve fitting to identify the value for minimum fluidization velocity, U_{mf}, and using the Ergun's equation to determine mean void fraction (ε). As an example, Figure 2-4 provides the pressure drop plot as a function of superficial gas velocity for LDPE particles. The total pressure drops (ΔP_{total}) is normalized by corresponding gravity caused pressure for the bed, namely mg/A, where A is the cross-sectional area of the bed, and mg is the total weight of the particles. As shown, there are two distinct regions representing fixed and fluidized states, and the transition point denotes U_{mf}. The determination of the transition point involves curve fitting as discussed in Tucker et al. (2013). Moreover, the point of the intersection corresponding to the minimum fluidization point shows a slightly less than one value, presumably due to the inner wall friction. Minimum fluidization velocity and associated mean void fraction and bulk density values of the fluffed bed are summarized in Table 2-2

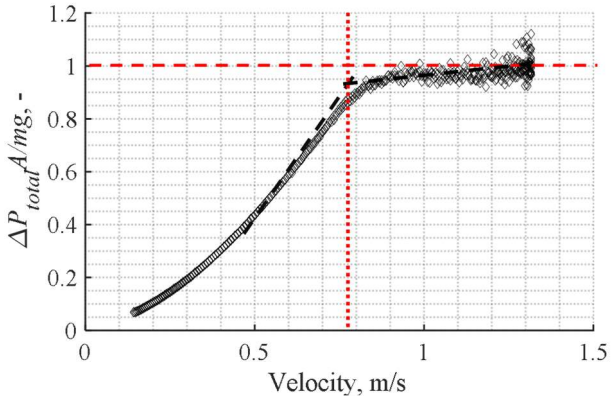

Figure 2-4: Sample pressure drop data as a function of superficial gas velocity for LDPE particles minimum fluidization test. The red dashed line indicates the pressure drop corresponding to the total weight, the black dashed lines show the curve fitting of the two distinct regions, and the dotted red line represents the Umf.

Table 2-2: Minimum fluidization velocity and associated mean void fraction and bulk density values of the fluffed bed.

Particle type	Mean Void Fraction	Bulk Density (g/cm^{-3})	U_{mf} (m/s)
Sand	0.468	1.377	0.245
Spherical LDPE	0.379	0.593	0.782
Wood	NA	NA	NA

2.3 FLUIDIZATION EXPERIMENTS

Fluidization experiments were performed using a cylindrical testbed having an internal diameter of 2.5", depicted in Figure 2-5. The schematic also shows the location of seven pressure ports used to measure differential pressure across the different locations of the bed. A total of seven 100-Hz high-speed pressure differential transducers (PDTs) are used to record temporal pressure fluctuation across the bed. The details of the measurement range in terms of axial locations and pressure sensor information is summarized in Table 2-2. Note, the total pressure ΔP is a redundant measurement to make sure the pressure ports behave properly during operations, namely:

$$\Delta P = \Delta P_1 + \Delta P_2 + \Delta P_3 + \Delta P_4 + \Delta P_5 + \Delta P_6 \quad (2\text{-}1)$$

Equation (2-1) is checked for all measurements during the data processing. Figure 2-6 provides a sample comparison of the left- and right-hand side of the equation using time series of the pressure data from the 3-inch LDPE pellets static bed and 100 wood pellets experiments at a superficial gas velocity of $3U_{mf}$. As expected, the two temporal signals match reasonably well, with the total pressure signal by summation slightly lower than the direct total pressure measurement possibly due to the connector pressure loss. High-Efficiency Particulate Air (HEPA) filters were equipped at the exit to trap possible overflow of particles and a distributor plate is placed between the two flanges connecting the plenum and the acrylic column. The plate is made out of sintered metal and is rated at 40 media grade (Mott Corp). The fluidization gas is supplied into the plenum chamber from a centralized air compressor system at the desired flow rate using an Alicat Scientific mass flow controller, with a range of 0 - 500 SLPM and accuracies of ±0.8% of reading + 0.2% of full scale. Differential pressure data were recorded for each test at least for a duration of 60s. In addition to pressure signals, solids bed height statistics, particles scale information, were measured using high-speed imaging as discussed below.

All fluidization tests are visualized and quantified using a Phantom v641-32G-Mag-M Complementary Metal Oxide Semiconductor (CMOS) high-speed camera, with a sensor size of 2560 by 1600 pixels and a physical pixel size of 20 μm. The aim of the high-speed recordings is to (1) visualize the fluidization process, (2) measure the temporal evolution bed height, and (3) extract particle scale information, including spatial distribution of particles, particle velocity and orientation, etc. The camera was equipped with both a 50-mm Nikon lens for bed height measurement and a 105-mm Nikon lens for particle scale measurement. Two measurements were conducted at 100 frames per second (fps), and 800 fps respectively. The lower magnification measurements (50-mm lens) records the full bed height range, whereas the higher magnification measurements (105-mm lens) records bed up to 16'', covering pressure port 1 – 6. The units were back lit by a Light Emitting Diode (LED) array mounted away from the bed and the light is diffused by a translucent paper. The photo of the fluidization experiment setup is provided in Fig 2-7, with all corresponding components marked. Leak tests were performed before and after the experiments and no leak was detected for all the test sections.

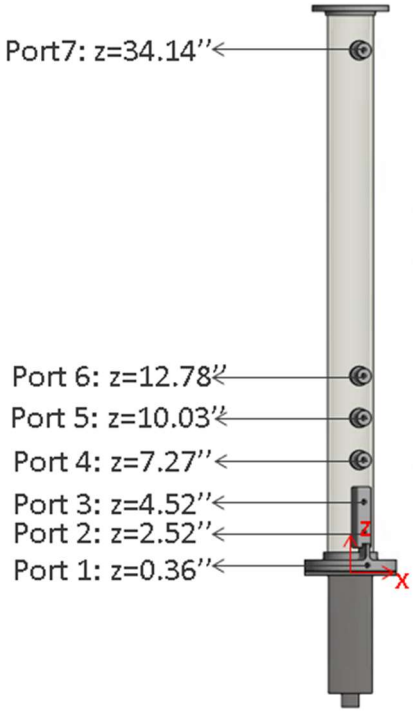

Figure 2-5: Schematic representation of test sections used in the current study having an inner diameter (ID) of 2.5".

Table 2-3: Pressure sensor configurations.

Pressure	Low pressure port	High pressure port	Range/ inch of H_2O	PDT number
ΔP1	1	2	±7.5	825
ΔP2	2	3	±7.5	823
ΔP3	3	4	±7.5	811
ΔP4	4	5	0- 5	801
ΔP5	5	6	0- 5	803
ΔP6	6	7	0- 5	815
ΔP	1	7	0- 30	809

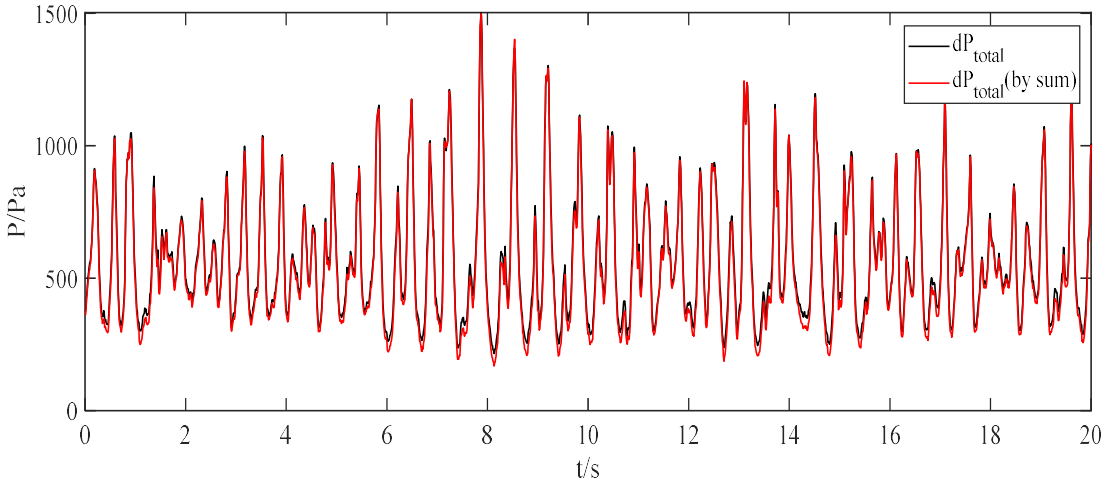

Figure 2-6: Comparison of total pressure measurement by direct measurement and by summation of partial pressure signals.

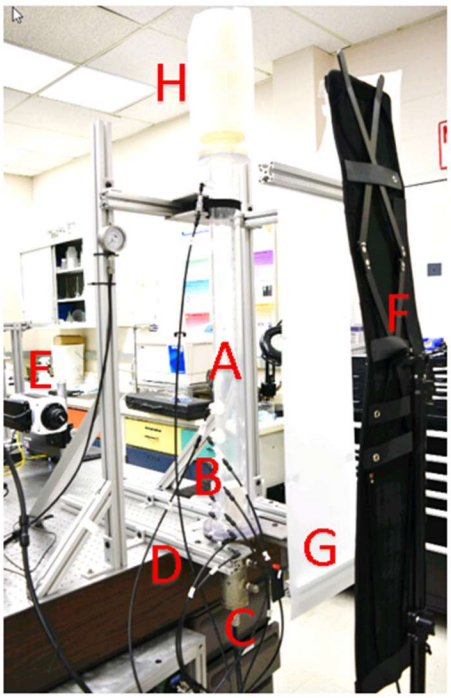

A – 2.5-inch diameter fluidized bed

B – Differential pressure sensors

C – Gas inlet

D – Porous distributor

E – Phantom V641 high speed camera

F – LED light panel

G – Diffuse paper

H - HEPA filter

Figure 2-7: Experimental setup of the fluidization tests.

2.4 PARAMETER SPACE

This section reports the major physical parameters for all binary or ternary mixing experimental runs, 64 runs in total. The experiments are categorized into three groups, namely, group 1 LDPE-wood mixing experiment, group 2 sand-wood mixing experiment, and group 3 sand-LDPE-wood mixing experiment. Tables 2-4 to 2-6 summarize the major physical and imaging information for experimental groups 1 to 3, respectively. The variation of the parameters aims to investigate the effects of initial bed height, wood particles fraction, as well as superficial gas velocity on the fluidization behavior of the binary or ternary mixing configurations. In general, for each run, data of pressure and bed height time series, particles spatial and velocity distribution, along with wood particle orientation are available for comparison. The data includes few transient runs, including Run 1, Run 28, and Run 51, all operated at $3U_{mf}$, where different types of particles are perfectly separated at time 0. We remark that the ranges of superficial gas velocity are different across different experimental groups and in the same group but different initial bed height. For example, the superficial gas velocity ranges from 1.5 U_{mf} to 3.7 U_{mf} for group 1, but 1.5 U_{mf} to 5 U_{mf} for group 2. Also, within group 1, the superficial gas velocity range is from 1.5 U_{mf} to 3.7 U_{mf} for 3'' initial bed height case, but is reduced to 1.5 U_{mf} to 3 U_{mf} for 6'' case. This is because the choice of the maximum superficial gas velocity is limited by (1) the physical dimension of the bed, and (2) the allowable maximum pressure in the laboratory, which is 1 atm. Throughout the report, we aim to elucidate the effects of the abovementioned quantities by varying one parameter at a time.

Furthermore, the attrition of wood particles is monitored in the experimental group 1 and 2 by recording the mass of wood particles before and after each experimental set. In all runs, the mass loss presumably due to attrition ranges from 0.47% to 6.23%. The maximum value is found in experimental group 2 for the 200 wood particles run at the highest fluidization velocity ($4U_{mf}$). The initial bed height is based on the component except for the wood particles. For example, for the group 1 experiment, the initial bed height is measured based on the LDPE particles in the bed, the wood particles are then added after the initial bed height is confirmed. The fluidization velocity is based on the minimum fluidization velocity of LDPE, sand and sand particles for the experimental group 1 to 3, respectively.

Table 2-4: Summary of experimental group 1, LDPE-wood mixing.

Group	Run #	Wood before (g)	Wood after (g)	Wood count	Sand mass (g)	LDPE mass (g)	Initial bed height (inch)	Flow rate	Frame rate
1	1	42	40.3	100	NA	149.3	3	3.0 U_{mf}	800
	2	42.7	40.3	100	NA	149.3	3	1.5 U_{mf}	800
	3	42.7	40.3	100	NA	149.3	3	2.0 U_{mf}	800
	4	42.7	40.3	100	NA	149.3	3	3.0 U_{mf}	800
	5	42.7	40.3	100	NA	149.3	3	3.7 U_{mf}	800
	6	42.7	40.3	100	NA	149.3	3	3.7 U_{mf}	800
	7	42.7	40.3	100	NA	298.6	6	1.5 U_{mf}	800
	8	42.7	40.3	100	NA	298.6	6	2.0 U_{mf}	800
	9	42.7	40.3	100	NA	298.6	6	2.0 U_{mf}	800
	10	42.7	40.3	100	NA	298.6	6	3.0 U_{mf}	800
	11	22.7	NA	50	NA	298.6	6	3.0 U_{mf}	800
	12	22.7	NA	50	NA	298.6	6	3.0 U_{mf}	800
	13	22.7	NA	50	NA	298.6	6	3.0 U_{mf}	100
	14	44.2	NA	100	NA	298.6	6	1.5 U_{mf}	100
	15	44.2	NA	100	NA	298.6	6	2.0 U_{mf}	100
	16	44.2	NA	100	NA	298.6	6	3.0 U_{mf}	100
	17	44.2	NA	100	NA	298.6	6	3.0 U_{mf}	100
	18	85.7	83.6	200	NA	298.6	6	3.0 U_{mf}	100
	19	85.7	83.6	200	NA	298.6	6	3.0 U_{mf}	100
	20	85.7	83.6	200	NA	298.6	6	3.0 U_{mf}	800
	21	85.7	83.6	200	NA	298.6	6	2.5 U_{mf}	800
	22	85.7	83.6	200	NA	298.6	6	2.5 U_{mf}	100
	23	20.9	NA	50	NA	298.6	6	2.5 U_{mf}	100
	24	20.9	NA	50	NA	298.6	6	2.5 U_{mf}	800
	25	43	42.8	100	NA	298.6	6	2.5 U_{mf}	800
	26	43	42.8	100	NA	298.6	6	2.5 U_{mf}	800
	27	43	42.8	100	NA	298.6	6	2.5 U_{mf}	100

Table 2-5: Summary of experimental group 2, sand-wood mixing.

Group	Run #	Wood before (g)	Wood after (g)	Wood count	Sand mass (g)	LDPE mass (g)	Initial bed height (inch)	Flow rate	Frame rate
2	28	42.9	42.2	100	364.5	NA	3	3.0 U_{mf}	400
	29	42.9	42.2	100	364.5	NA	3	1.5 U_{mf}	800
	30	42.9	42.2	100	364.5	NA	3	1.5 U_{mf}	100
	31	42.9	42.2	100	364.5	NA	3	2.0 U_{mf}	100
	32	42.9	42.2	100	364.5	NA	3	2.0 U_{mf}	800
	33	42.9	42.2	100	364.5	NA	3	3.0 U_{mf}	800
	34	42.9	42.2	100	364.5	NA	3	3.0 U_{mf}	100
	35	42.9	42.2	100	364.5	NA	3	4.0 U_{mf}	100
	36	42.9	42.2	100	364.5	NA	3	4.0 U_{mf}	100
	37	42.9	42.2	100	364.5	NA	3	4.0 U_{mf}	800
	38	42.9	42.2	100	364.5	NA	3	5.0 U_{mf}	800
	39	42.9	42.2	100	364.5	NA	3	5.0 U_{mf}	100
	40	42.9	42.2	100	364.5	NA	3	NA	100
	41	21.7	NA	50	729	NA	6	4.0 U_{mf}	100
	42	21.7	NA	50	729	NA	6	4.0 U_{mf}	800
	43	42.6	NA	100	729	NA	6	1.5 U_{mf}	100
	44	42.6	NA	100	729	NA	6	1.5 U_{mf}	800
	45	42.6	NA	100	729	NA	6	2.0 U_{mf}	100
	46	42.6	NA	100	729	NA	6	3.0 U_{mf}	100
	47	42.6	NA	100	729	NA	6	3.0 U_{mf}	800
	48	42.6	NA	100	729	NA	6	4.0 U_{mf}	100
	49	42.6	NA	100	729	NA	6	4.0 U_{mf}	800
	50	85.1	79.8	200	729	NA	6	4.0 U_{mf}	100

Table 2-6: Summary of experimental group 3, sand-wood-HDPE mixing.

Group	Run #	Wood before (g)	Wood after (g)	Wood count	Sand mass (g)	LDPE mass (g)	Initial bed height (inch)	Flow rate	Frame rate
3	51	0	NA	NA	364.5	42.9	3	3.0 U_{mf}	800
	52	0	NA	NA	364.5	42.9	3	1.5 U_{mf}	100
	53	0	NA	NA	364.5	42.9	3	1.5 U_{mf}	800
	54	0	NA	NA	364.5	42.9	3	2.0 U_{mf}	100
	55	0	NA	NA	364.5	42.9	3	2.0 U_{mf}	800
	56	0	NA	NA	364.5	42.9	3	3.0 U_{mf}	100
	57	0	NA	NA	364.5	42.9	3	3.0 U_{mf}	800
	58	0	NA	NA	364.5	42.9	3	4.0 U_{mf}	100
	59	0	NA	NA	364.5	42.9	3	4.0 U_{mf}	800
	60	10.7	NA	25	364.5	10.7	3	3.0 U_{mf}	100
	61	21.4	NA	50	364.5	21.4	3	1.5 U_{mf}	100
	62	21.4	NA	50	364.5	21.4	3	2.0 U_{mf}	100
	63	21.4	NA	50	364.5	21.4	3	3.0 U_{mf}	100
	64	42.9	NA	100	364.5	42.9	3	3.0 U_{mf}	100

2.5 IMAGING AND DATA PROCESSING

All the image-based 2D measurements in this report are performed along the x-z plane as shown in the schematics Figure 2-5. As discussed in section 2.3, the higher frame rate and higher spatial resolution case are used for particles velocity or orientation extraction, whereas the lower frame rate and lower spatial resolution recordings are applied for temporal bed height measurement. The technical details are summarized in Table 2-7.

To extract the temporal evolution of the expanded bed height, we employ the method used in Gao et al. (2020). Briefly, the images processing steps include three phases, namely, (1) crop the image to identify the region of interest, (2) global thresholding using the Otsu method, and (3) morphological filtering to remove objects that do not belong to the moving particles, for example, the particles sticking to the wall due to electrostatic force.

Table 2-7: Imaging parameters for bed height and particle velocity/orientation measurement.

	Frame rate/ Hz	Spatial resolution/ cm per pixel	Time resolution/ sec per frame	FOV/cm^2
Bed height measurement	100	0.0367	0.01	94.0 x 29.4
Particle velocity/orientation measurement	800	0.0168	0.00125	43.0 x 13.4

The time-resolved (800 Hz) particle images series are used to perform simultaneous Particle Image Velocimetry (PIV) on LDPE or/and sand particles, and Particle tracking velocimetry (PTV) on the wood pellets. The processing involves three phases: (a) segmentation of particles and background, (b) generate particle images containing only one component (c) perform PIV or PIV on the corresponding image. Figure 2-8 illustrates the segmentation and identification of wood particles. The raw images are cropped into regions of interest as shown in Figure 2-8a.

The next step is the segmentation step where the cropped image is segmented into background and different particle types. Most traditional segmentation methods are based on the intensity and/or the spatial relationships of pixels, whereas human's manual segmentation is more complicated and usually proves to be more effective. However, manual segmentation is time-consuming and is inefficient in processing large image data sets as we have it here (c.f. Table 2-4 to 2-6). To automatically distinguish between the different particle types, and the background, the Trainable Weka Segmentation (TWS) tool is applied (Arganda-Carreras et al. 2017). It is a machine learning tool initially designed for microscopy pixel classification and is distributed as an open-source software package as part of the Fiji image processing distribution of ImageJ (Ferreira & Rasband 2011). This tool has been used in a wide range of applications such as cell segmentation (Araújo et al. 2019), tissue segmentation (Polan et al. 2016), crystal size distributions (Lormand et al. 2018). TWS is capable of train a pixel classifier and segment the remaining image dataset automatically, with a limited number of manual annotations. Moreover, TWS contains a wide selection of image features including various edge detectors, texture filters, and noise reduction filters, and users are able to select and tune associated parameters. Figure 2-8b provides a sample image of the segmented results, where the red, green, and purple pixels represent wood pellets, LDPE particles, and the background, respectively. Figure 2-8c shows the generated mask for wood particles and Figure 2-8d presents a filtered version of wood particles where noise is removed. Finally, the individual wood particles from the resulting black-white image are detected (Figure 2-8e) and the properties such as centroid, eccentricity, orientation, major/minor axis length, etc., are measured. Note, the current measurement is in 2D, the measured orientation is defined as the angle between the positive z axis (θ_z) (c.f. Figure 2-5) projected onto the x-z plane, denoted as $\theta_{z\text{-}xz}$. Due to projection, we always have: $\theta_z \geq \theta_{z\text{-}xz}$. All current data processing is processed by TWS.

Additionally, an in-house Python machine learning (ML) code has also been developed for image segmentation. The goal of implementing ML for analysis has three primary components which are to reduce image processing time over manual methods, improve accuracy over other types of methods such as TWS, and to provide a better pipeline for processing additional images that may or may not be similar to images utilized for this project. The code was written using Python version 3.8.5 that leverages Artificial Intelligence (AI) with a pre-trained Neural Network called VGG16 on the ImageNet dataset and then utilizes traditional machine learning to include Random Forest and Gradient Boosted Tree models for prediction. Image segmentation differ from image classification because the image type is not necessarily known. Segmentation therefore attempt to classify each individual pixel with a specific pixel known as a label value. By classifying each individual pixel of an image, image segmentation models can recreate an image by attempting to predict the pixel label based upon the features available for prediction. For this process to work properly there must be images that the model can use to train and mage masks which are images that must be manually labeled so that the machine learning model can have a response variable. In

this case, the mask creation is time consumin. Each pixel in the mask does not need to be labeled; however, each image mask used for training must include labels for all interested pixels. In our model, we have image pixels valued from 1-3 with each value assigned to a specific particle, namely pixel value 1 representing wood pellets, pixel value 2 representing LDPE particles, and pixel value 3 representing the background.

The VGG16 model was used to as a feature extractor for the training images. By utilizing the first layer of the VGG16 model there are 64 features generated per image. Each feature has a weighted value and therefore, one pixel on an image will have 64 features and a single pixel value that is given by the mask. These 64 features become the predictors for ML models and the label is the actual pixel value. This method of using a neural network as a feature extractor for ML models works better than a neural network alone when there are insufficient quantities of training images and masks. In our case, we had 26 training images and masks. The training data was randomly divided into 18 images for training and 8 images for testing. There were three models utilized for training and each model was tuned for the best performance. Because of the volume of images that this model will be used to predict, both accuracy and prediction time are important. The best performing model using feature from VGG16 is XGBoost, which is an extreme gradient boosting tree-based model. The XGBoost model not only had the best accuracy scores but also had the fastest prediction times. For accuracy, it is important to measure the entire accuracy of the model which is how well the model can label each pixel. However, it is more important to understand how well the model labels pixels of each value. For example, in our dataset, pixels labeled 1 were the wood particles. It is important to see how well the model is predicting pixel 1 specifically. For this computation, we used Intersection over Union (IoU) to determine how well each pixel was predicted and specifically focused on pixels of value 1. Table 2-8 provides a comparison of the model performance.

Table 2-8: Comparison of model performance.

Model	Total Accuracy	Pixel 1 Accuracy	Time to Predict 10 Images
XGBoost	97.59%	67.96%	0.23 minutes (14 seconds)
Random Forest	96.40%	55.99%	17 minutes
SVM	96.66%	56.31%	1,803 minutes (30.5 hours)

The particle tracking algorithm by Ouellette et al. (2006) is applied to the detected wood particle centroid to extract the Lagrangian particle trajectories. Sample wood particle trajectories are shown in Figure 2-9. To extract the Eulerian velocity field by PIV, the wood particles are then masked out in the original image, and only LDPE or/and sand particles are left. The resulting particle images are processed using a MATLAB-based PIV (Thielicke & Stamhuis 2014) software PIVLAB for the extraction of LDPE or/and sand particle velocity field. The processes discussed above are illustrated in Figure 2-10.

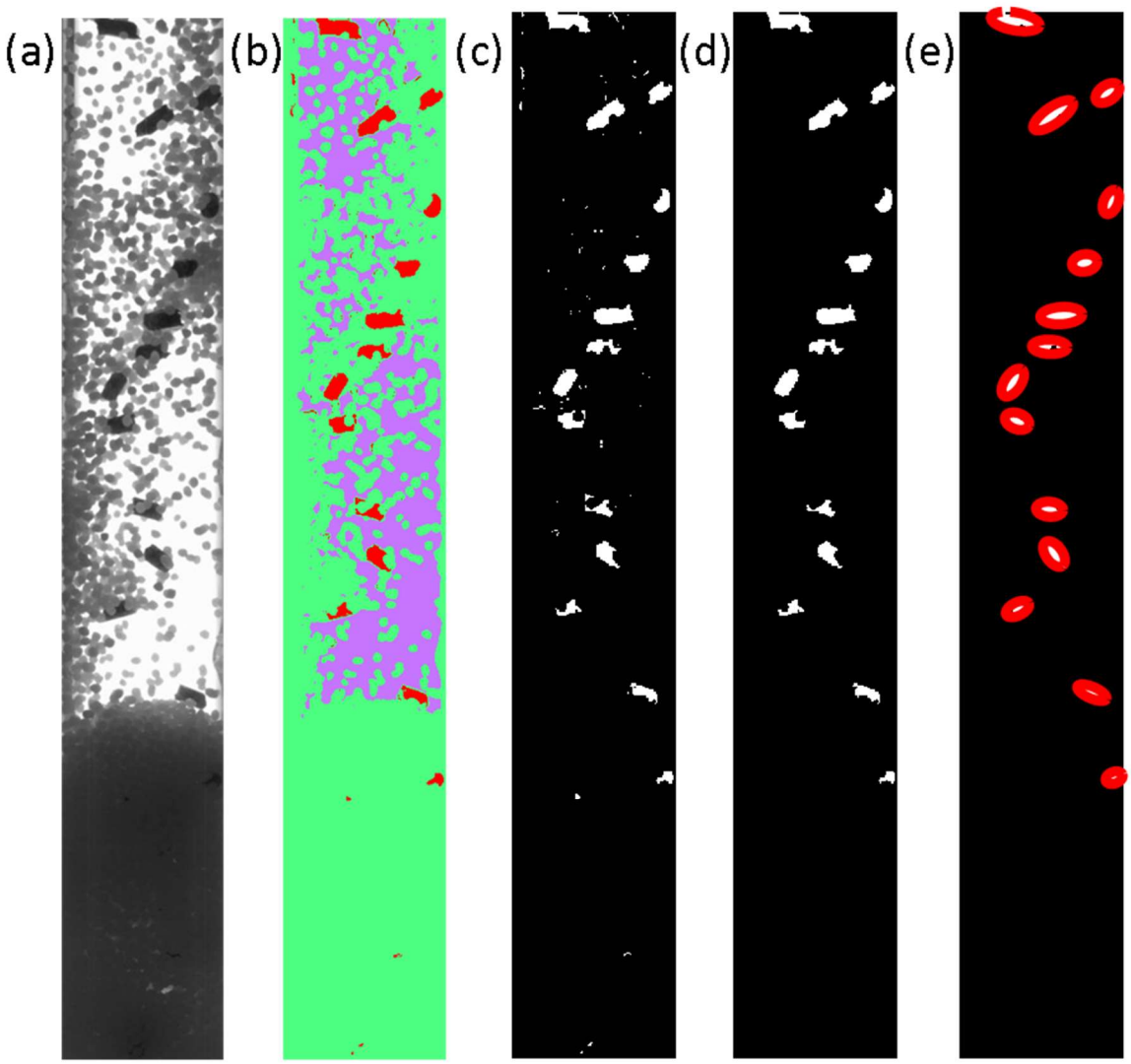

Figure 2-8: Segmentation of particles. (a) raw particle image, (b) machine learning segmentation results, (c) segmented wood particles, (d) segmented wood particles after noise filtering, and (e) detected wood particles.

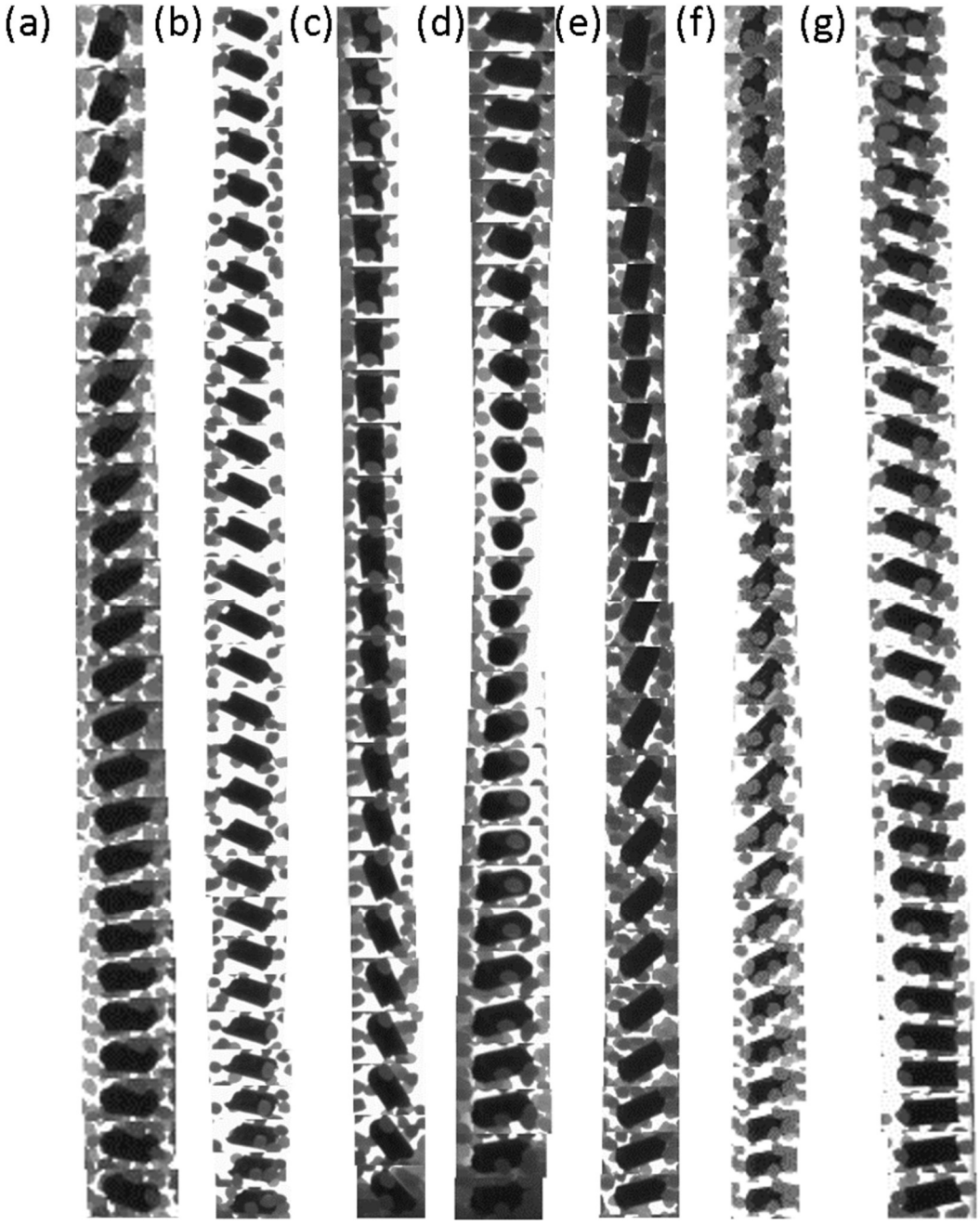

Figure 2-9: Sample of wood particle trajectories of LDPE and 100 wood pellets experiment, at 3 Umf.

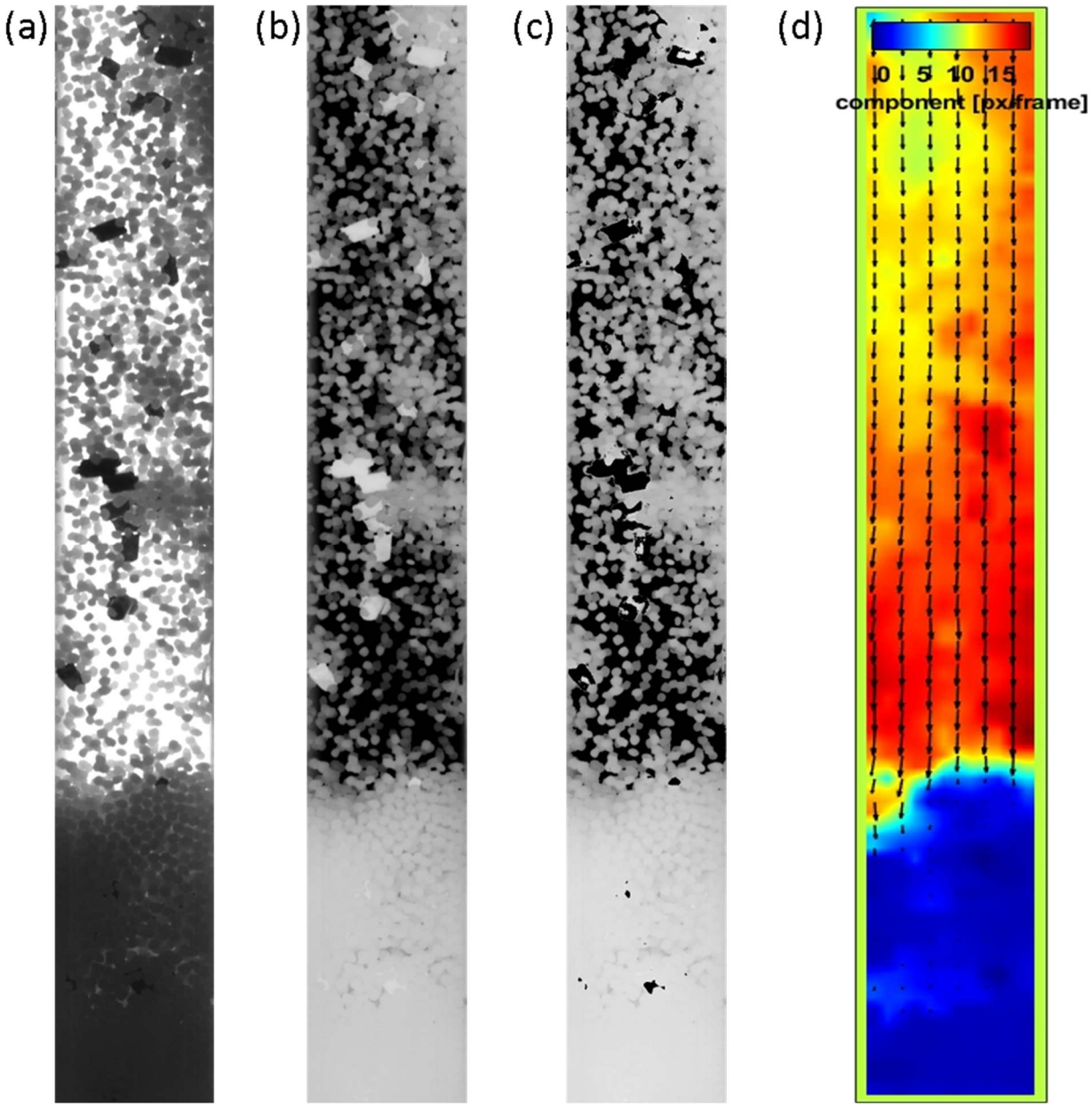

Figure 2-10: Steps involved in calculating the velocity field of LDPE particles. (a) raw image, (b) intensity inverted image, (c) image with detected background and wood particles set to black, (d) Eulerian velocity field of LDPE after PIV processing.

3. RESULTS

3.1 SPHERICAL LDPE PARTICLE FLUIDIZATION

Before investigating the binary/ternary fluidization behavior, single component fluidization experiments are performed to provide baseline information. For all cases, the static bed height is 7.62 cm, consisting of 149.3 g of spherical LDPE particles. The superficial gas velocities investigated include 1.4 U_{mf}, 2.0 U_{mf}, 3.0 U_{mf}, 3.4 U_{mf}. Figure 3-1 provides a series of sample images from the spherical LDPE particle fluidization experiment. As shown, the expanded bed height increases with the superficial gas velocity from 1.4 U_{mf} to 2.0 U_{mf}. At 2.0 U_{mf}, the so-called flat slug flow is formed due to the relatively narrow bed configuration. Figure 3-2 shows the different stages of the slugging flow. Figure 3-2a shows the starting of forming slugs as the bed separates into slices of particles separated by gas. In Figure 3-2b, the gas filled in more space as the slug increase in volume and lift the particle slug upward. As this process continues, the top slice of particles begins to unreplenish by raining particles as shown in Figure 3-2c. And Figure 3-2d shows the end of the unreplenishment of the top slice of particle slugs and the start of another slug.

With the further increase to 3.0 U_{mf} and 3.4 U_{mf}, such periodic slug flow motion disappears, and the expanded bed height remains almost unchanged and the bed top forms a quasi-steady fountain structure. The samples of temporal bed height evolution are provided in Figure 3-3 and the mean and fluctuation of the bed height for all four fluidization velocities are shown in Figure 3-4. As expected, the bed height fluctuates over time for all fluidization velocities as gas phase forms bubbles and burst as they reach the top of the bed. However, the resulting fluctuation intensity and the mean bed height differs. Both the mean and the fluctuation of the bed height increases from 1.4Umf (bubble bed) to 2.0 Umf (slug bed). With the increase of fluidization velocity from 2 Umf to 3Umf, both the mean and the fluctuation of bed height decrease due to the onset of spouted bed behavior at 3Umf. With a further increase of fluidization velocity to 3.4 Umf, the mean bed height increases, whereas the fluctuation of bed height decreases indicating a more stable spouted bed behavior. The transition of bubble/slug bed to spouted bed has been investigated before but was limited to configurations with a specialized spouting gas nozzle (Zhong et al. 2006). Detailed information on the spouted bed behavior using only porous distributor plate configuration for Geldart D particles is worth further investigation. And further numerical simulations under the same test condition are valuable to confirm the capability of the numerical model to capture the transition from bubble bed to slug bed, and finally to spouted bed.

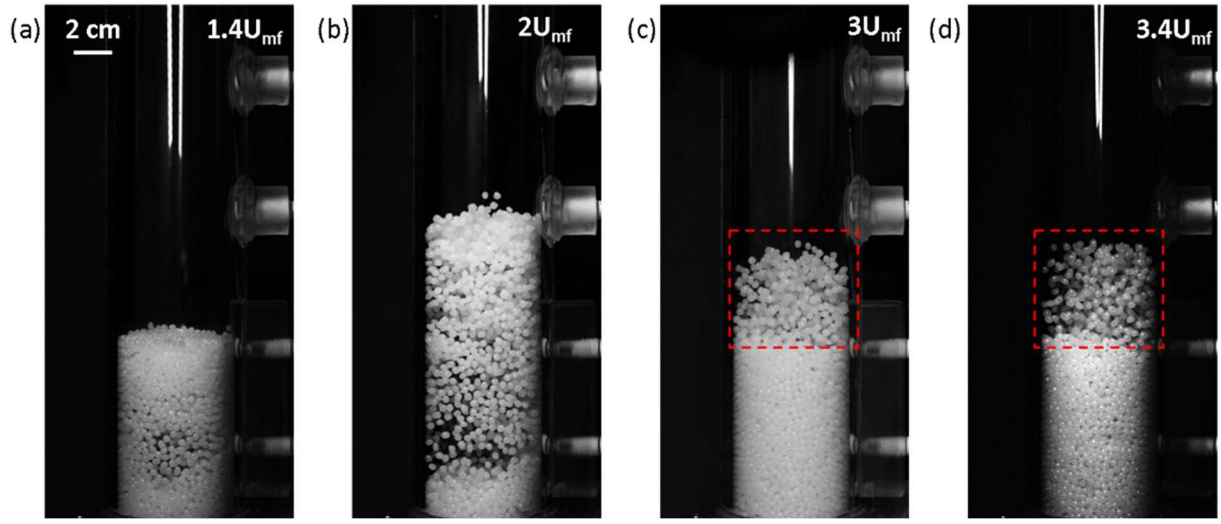

Figure 3-1: Spherical LDPE particle fluidization with superficial gas velocity from 1.4 – 3.4 U_{mf}. The dashed red rectangles in (c) and (d) correspond to the regions of a quasi-steady fountain.

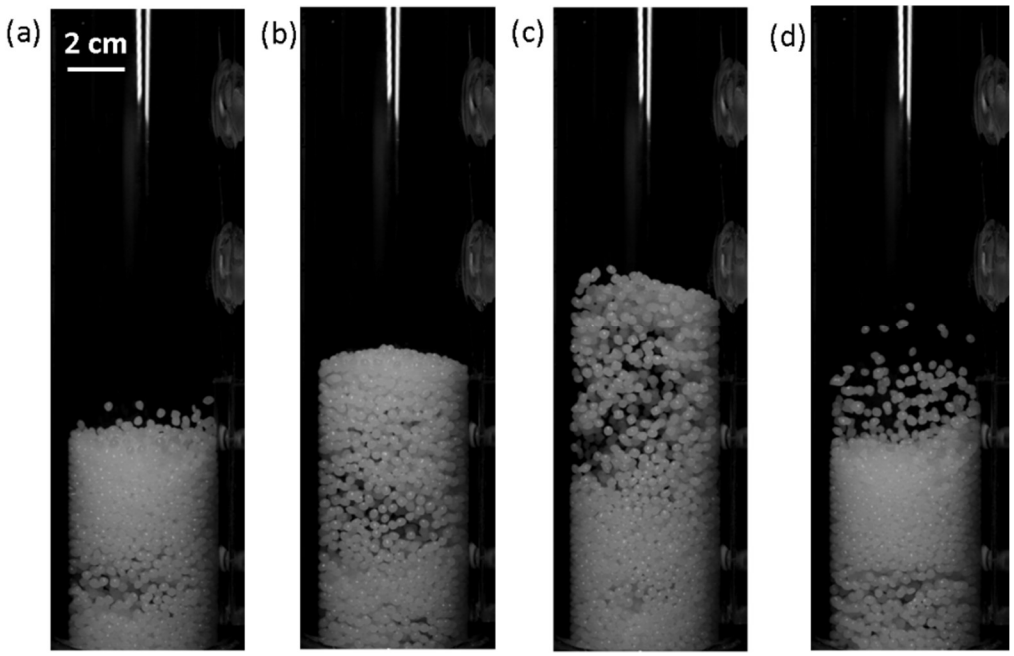

Figure 3-2: Formation of slug flow at $2U_{mf}$ for spherical LDPE particle.

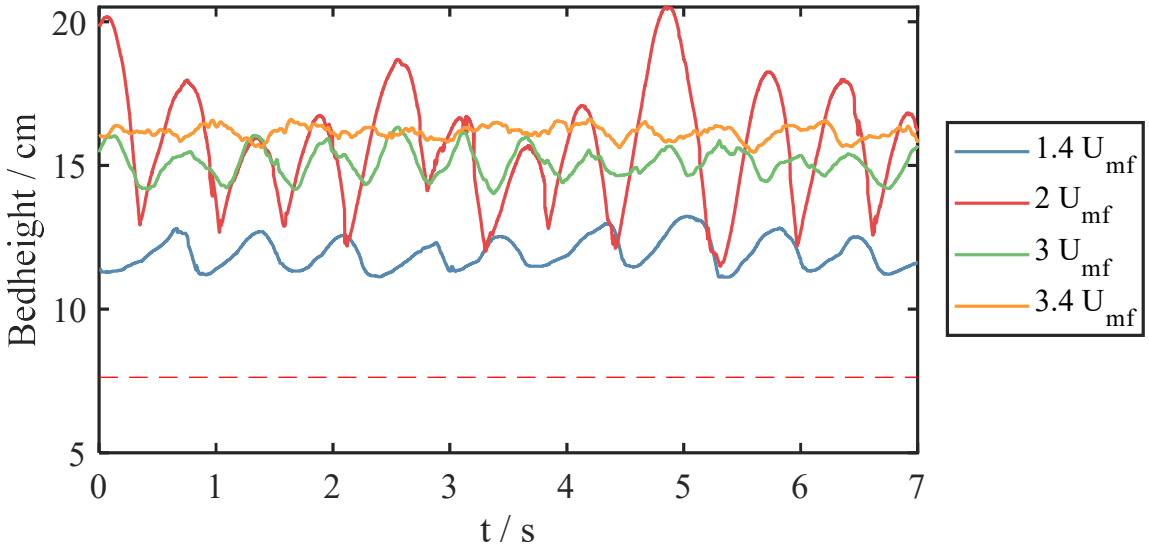

Figure 3-3: Sample temporal evolution of bed height for LDPE particle fluidization with the superficial gas velocity of 1.4 – 3.4 U_{mf}. The dashed red line indicates the static bed height.

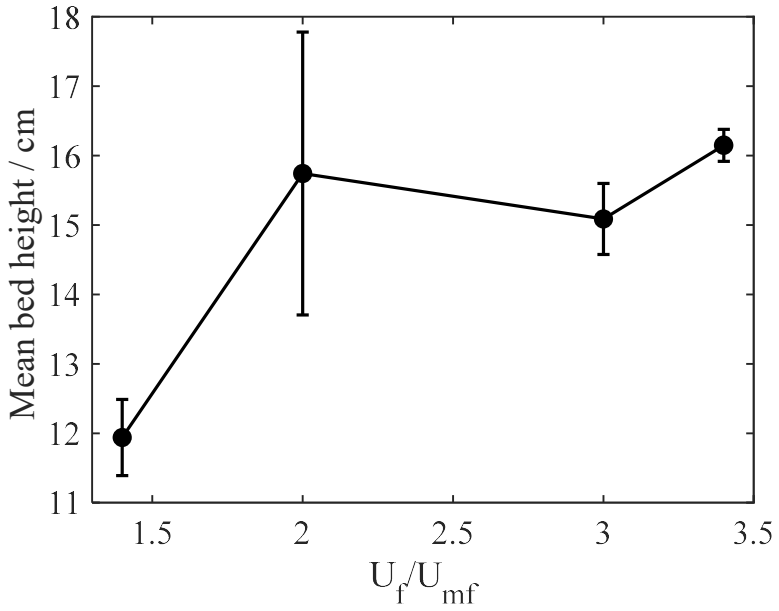

Figure 3-4: Mean bed height of LDPE particle as a function of fluidization velocity from 1.4 to 3.4 U_{mf}. The error bar indicates the standard deviation of the bed height time series.

3.2 BINARY FLUIDIZATION OF LDPE AND WOOD PARTICLES

This section summarizes the experimental results of binary fluidization of the spherical LDPE and cylindrical wood particles. The detailed parameter space has been summarized in Table 2-4 of section 2.4. The investigated variables include the static bed height, fluidization velocity, and wood particle fraction.

3.2.1 Transient mixing

The transient mixing behavior of wood and LDPE particles is investigated at a fluidization velocity of 3 U_{mf}. The U_{mf} is based on the LDPE particles. The static bed height of LDPE particles was kept at 7.62 cm corresponding to 149.3 g of LDPE particles and 100 wood pellets with $AR = 2$ were added to the LDPE bed. Both 100 Hz high-speed pressure data and 800 Hz high-speed video have been recorded immediately before the start of the flow to the steady-state of the fluidization. Figure 3-5 provides the time series of the initial mixing of the binary fluidization from 0 – 2173 ms. A slug composed of both wood particles on the top and LDPE particles at the bottom is formed immediately after the flow is supplied as shown in Figure 3-5b. Different from one component Geldard D solids slug flows, where the topmost slice of the particles are unreplenished through raining solids, and eventually disappear (Kunii & Levenspiel 1991), only the LDPE particle portion of the slug starts to disintegrate from the slug yet the wood pellets portion of the slug remains (Figure 3-5c) and falls as a particle cluster into the bottom of the bed as shown in Figure 3-5d. The gas flow then brings up the wood pellets and mix them with the LDPE particles. Note the LDPE and wood particles are fairly well mixed after around 2 seconds (Figure 2-5e)

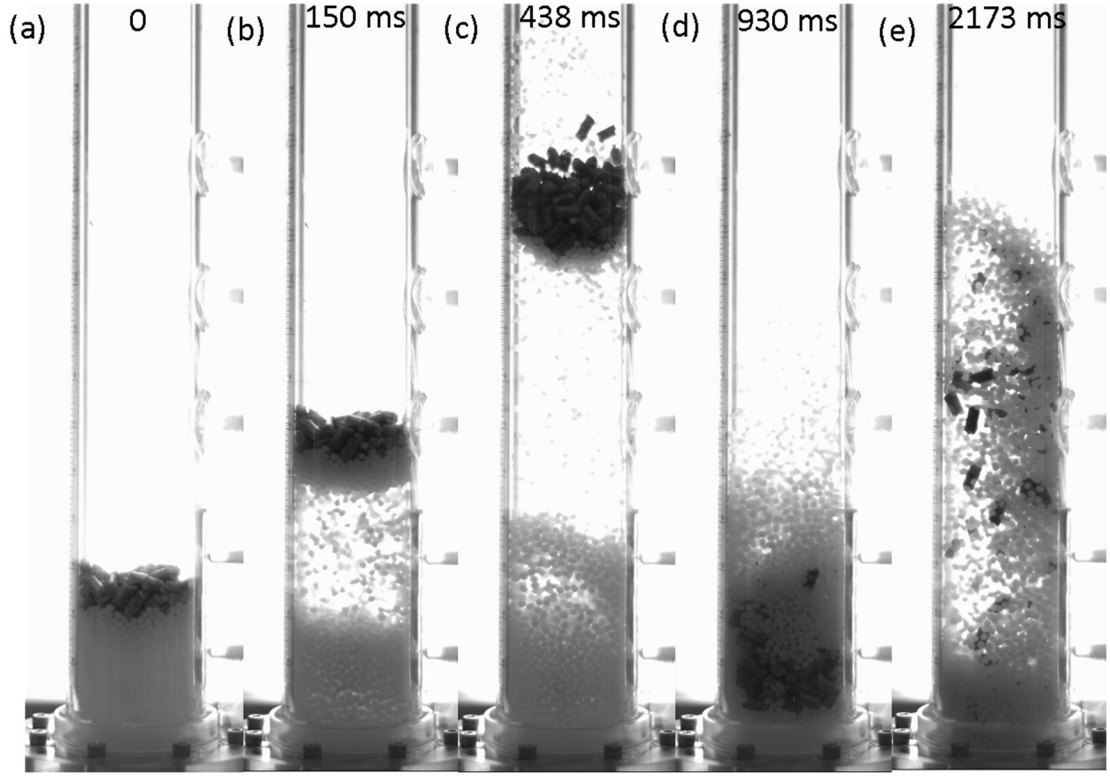

Figure 3-5: Time series of initial mixing of the wood and LDPE particles. The time after the start of the flow is labeled on the top of each sub-images of (a) to (e).

Figure 3-6 shows the total pressure drop as a function of time. Both the direct measurement (black line) and the total pressure measurement by summation of each measurement interval (red line) are shown with reasonable agreement. The mean pressure of total pressure is 568.2 Pa and 546.3 Pa for two measurements, respectively. The transient mixing signature is clearly observed for the first 1 second of the pressure signal.

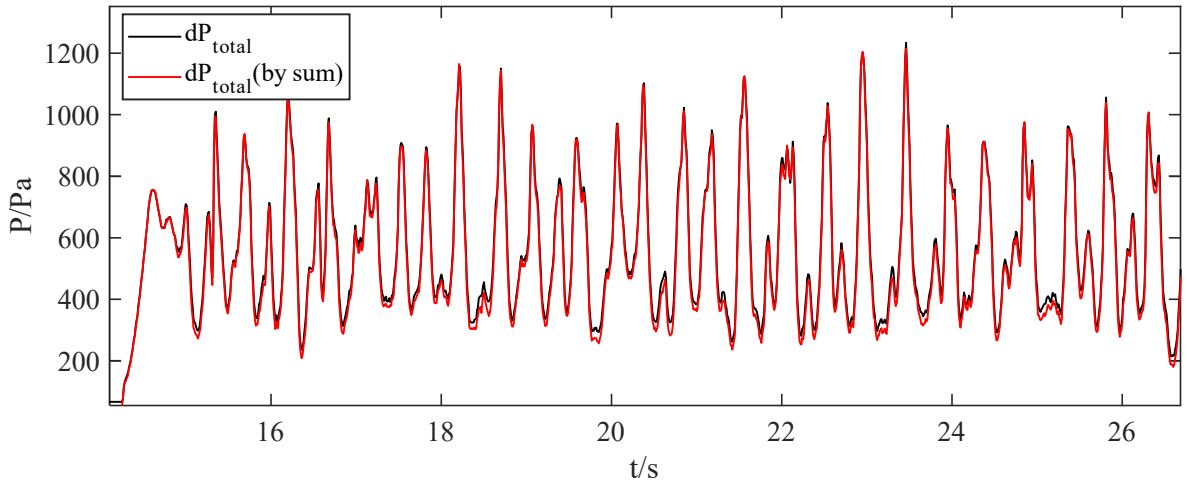

Figure 3-6: total pressure signal time series for transient mixing of LDPE and 100 wood pellets at 3 U_{mf}.

3.2.2 Effects of biomass fraction

The effects of biomass fraction are investigated by varying the wood pellets fraction at 50 particles, 100 particles, and 200 particles. The corresponding particle masses are 20.9 g (0.418 g/particle), 42 - 44.2 g (0.42 -0.442 g/particle), and 85.7 g (0.429 g/particle). The slight variation in mass per particle value is presumably due to the cutting imperfection for the AR = 1:2 particles. However, the maximum variation for mass per particle value is within 6%. For all cases, 298.6 g of LDPE particles are used, corresponding to a static bed height of 15.24 cm.

Sample images of the fluidization experiment at 3 U_{mf} are shown in Figure 3-7 with the AR=2 wood particle numbers ranging from 50 - 200. The corresponding mean and standard deviation of the total pressure drop for both 2.5 U_{mf} and 3.0 U_{mf} are shown in Figure 3-8. As expected, with the increase number of wood particles, the total weight of the material increases, and thus the total pressure drops increases during fluidization at both 2.5 U_{mf} and 3.0 U_{mf}. Moreover, the standard deviation of the total pressure drops time series increase with the increase of the wood particle number at both fluidization velocities. This is possibly due to the fact that with addition of more non-spherical particles in the system, the flow becomes more anisotropic and causing larger fluctuations in pressure drop. Further investigation is needed to confirm this assumption. The pressure power spectrum density (PSD) for the total pressure drop time series data have been calculated using the Fast Fourier Transform (FFT) and is shown in Figure 3-9. The PSD peak frequency slightly decreases with the increase of biomass fraction at both fluidization velocities. For example, at 2.5 U_{mf}, the peak frequency for 50 wood particle case is around 1.42 Hz, and 1.27 Hz for both 100 and 200 wood particle case. At the same U_{mf}, the peak amplitude of PSD increases with the increase of biomass fraction signifying a more intense slugging pattern. At 3 U_{mf}, the 50

wood pellets case, PSD peaks become weaker signifying the transition to spouting. This observation is qualitatively consistent with the high-speed video.

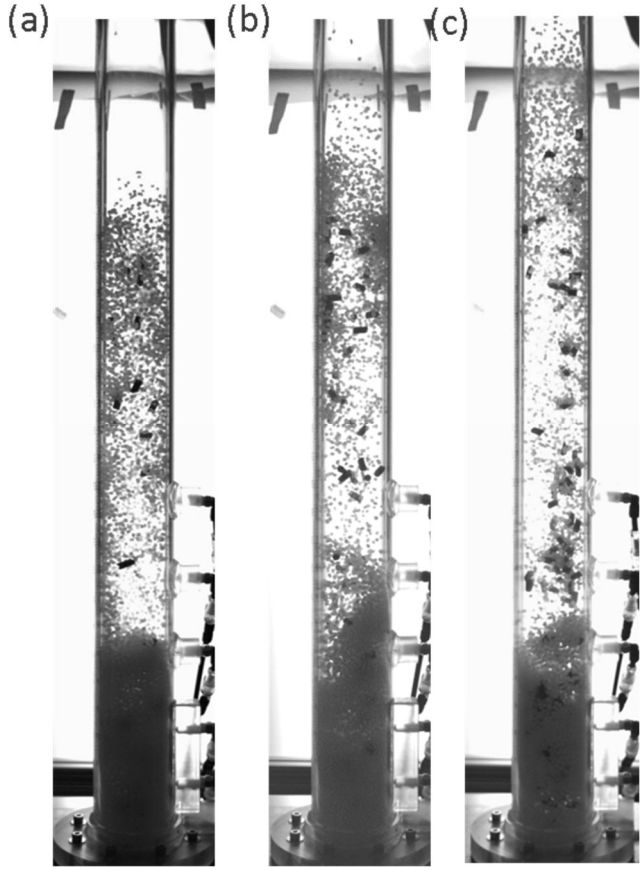

Figure 3-7:Sample image with varying biomass fraction at 3Umf. (a) 50 pellets, (b) 100 pellets, (c) 200 pellets.

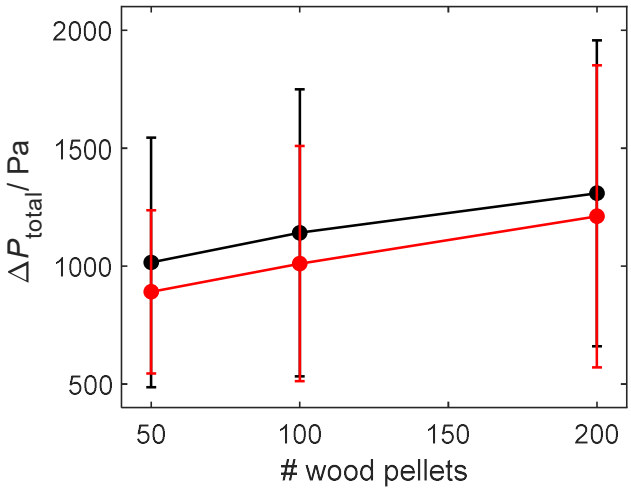

Figure 3-8: Mean and standard deviation of total pressure drop at 2.5 U_{mf} (red), 3.0 U_{mf} (black).

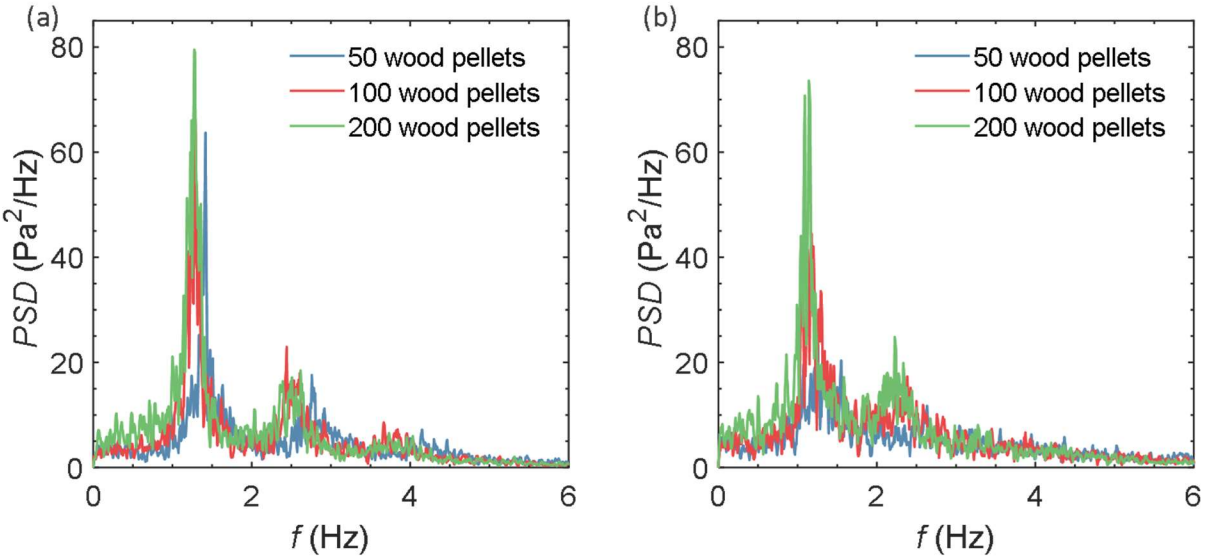

Figure 3-9: Effects of biomass fraction on the power spectrum density of the pressure signal (a)U_f/U_{mf}=2.5; (b) U_f/U_{mf}=3.

The bed height statistics have also been processed to compare cases with varying wood particle fractions. Figure 3-10 and Figure 3-11 shows the sample bed height time series at 2.5 U_{mf} and 3.0 U_{mf}, respectively. The mean and standard deviation of the bed height for all cases are summarized in Figure 3-12. As can be seen, the trend is different from the mean and standard deviation plot of pressure data (c.f. Figure 3-8). At 2.5 U_{mf}, the mean bed height increases with the increase of wood particles, however, at 3.0 U_{mf}, the mean bed height peaks at 100 wood particles. The result is consistent with the high-speed video by observation. The reason is possibly related to partial spout behavior as observed in pure LDPE particles (c.f. Figure 3-4). The standard deviation of the bed height is similar for all cases, ranging from 11.4 - 14.2 cm without clear trends. The bed height power spectrum density is provided in Figure 3-13. As expected, the shape resembles the pressure PSD in Figure 3-9, namely the trend of peak frequencies' locations is similar, indicating a slugging flow pattern.

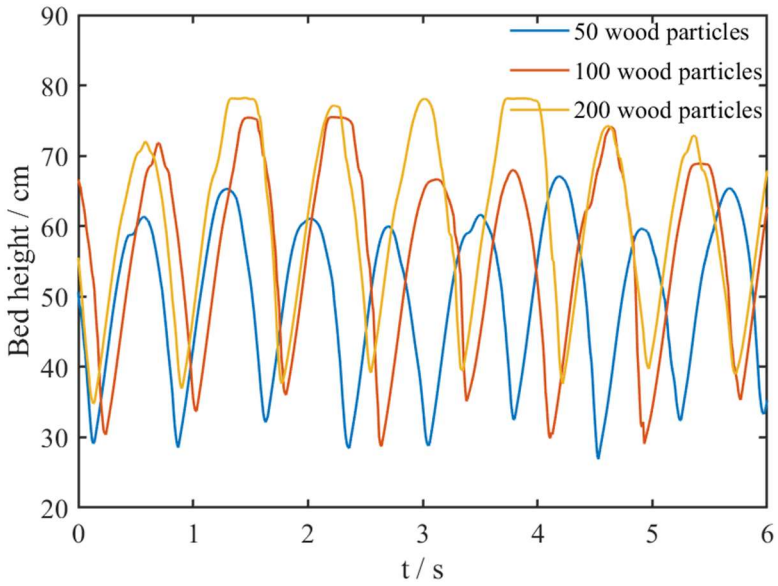

Figure 3-10:Sample time series of bed height with varying wood particle fraction at 2.5 U_{mf}.

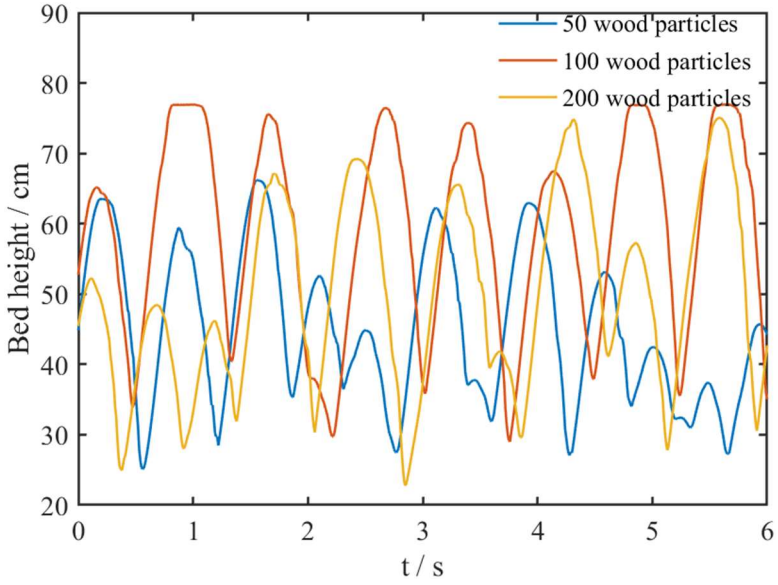

Figure 3-11: Sample time series of bed height with varying wood particle fraction at 3 Umf.

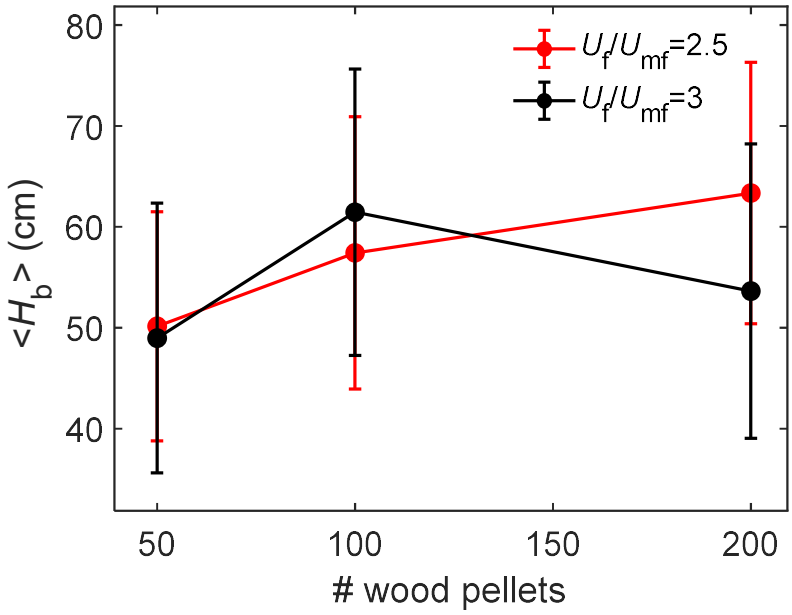

Figure 3-12: Mean and standard deviation of bed height measurements.

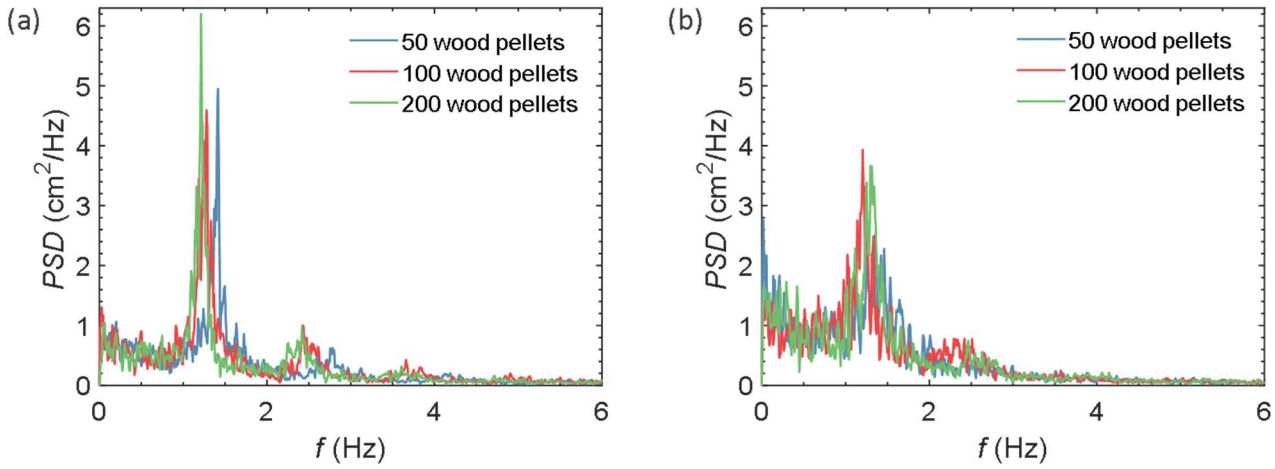

Figure 3-13: Effects of biomass fraction on the power spectrum density of the pressure signal (a)U_f/U_{mf}=2.5; (b) U_f/U_{mf}=3.

As discussed in section 2.5, higher spatial and temporal resolution recordings are acquired for the measurement of the wood particle orientation and particle velocity field measurement. In the remainder of this section, the results of the particle's velocity and orientation statistics are provided. The wood particles orientation distribution is shown in Figure 3-14 comparing the effects of wood pellets fraction, ranging from 50 - 200 counts. The orientation shown here is defined as the angle between the height of the particle and the z-axis projected onto the x-z plane, with ranges from 0 to 90°. For all three cases, the orientation PDFs all have a V-shape, with the dip in around 45°. The variation between runs seems to be minimal. The higher values of PDF at 0° is possibly due that the sampled particles tend to lie down when hitting the pool of LDPE particles, whereas particles tend to position vertically when bringing up by the air or falling. The velocity distribution of the detected particles is shown in Figure 3-15. For the horizontal velocity, the distributions are well presented by a normal distribution mean of around 0, and an increasing standard deviation with the increase of wood particle fraction.

The probability density function of both horizontal and vertical velocity for LDPE particles are shown in Figure 3-16. Different from wood particle velocity extraction using Lagrange tracking, i.e. PTV, these velocity distributions are acquired using images cross-correlation-based PIV method. Each PDF is based on all the velocity vectors from over 5000 velocity maps, each containing 70 x 9 vectors, providing statically robust results. The velocity distribution trends for wood and LDPE particles generally resemble each other. Interesting to note, the horizontal velocity standard deviation for LDPE particles is slightly lower than that for wood particles and thus the peak PDF value is higher for LDPE particle PDFs (c.f. Figure 3-15a and 3-16a). This is possibly due to the large pool of resting particles containing very small velocities, namely less fluidized caused by the nature of Geldard D type particles. This feature of enhanced zero velocity particles is also observed in Figure 3-16b. Moreover, the trends of the bimodal nature, as well as the relative intensity of both modes, match for both particles.

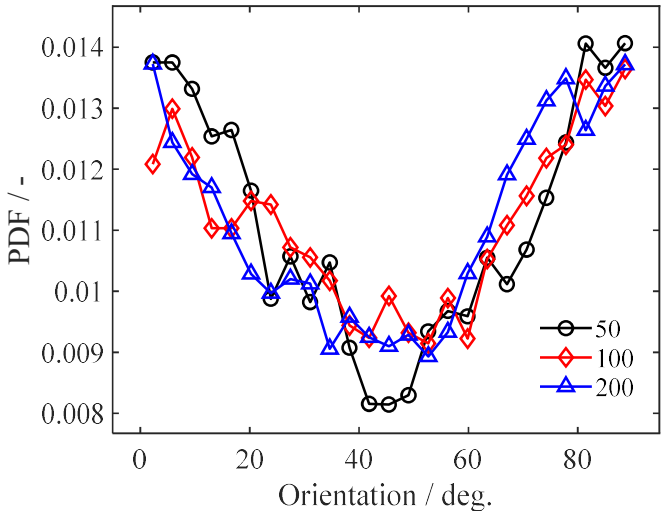

Figure 3-14: The probability density function of overall wood particle orientation at $3U_{mf}$ with varying wood particle counts.

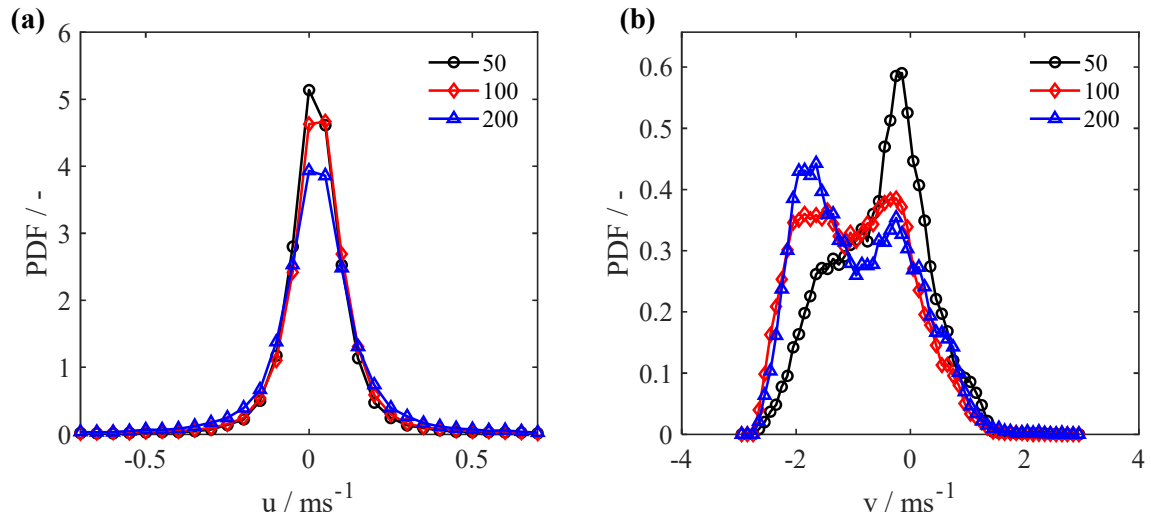

Figure 3-15: The probability density function of wood particles using PTV analysis: (a) horizontal velocity and (b) vertical velocity.

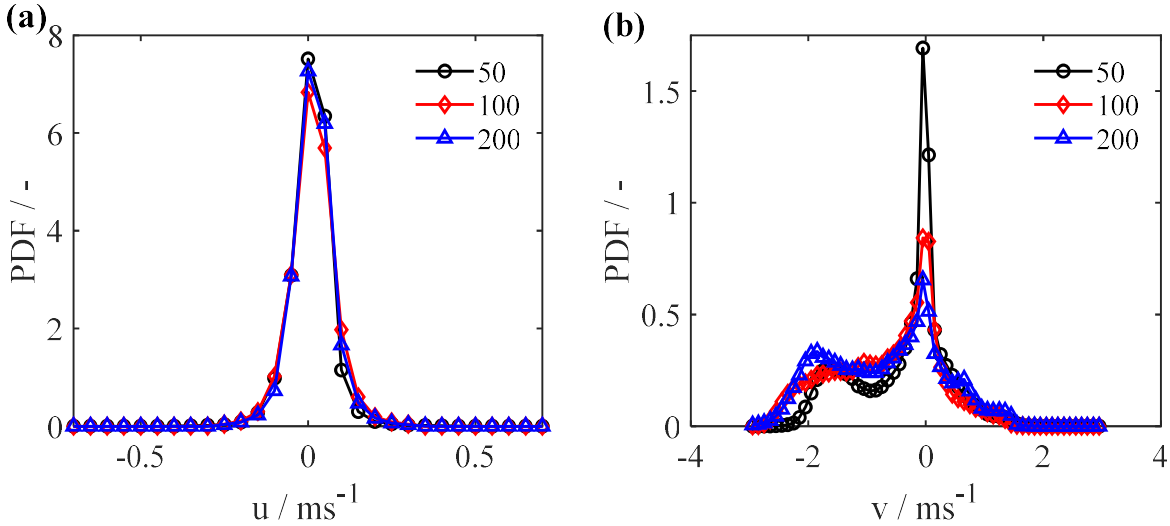

Figure 3-16: The probability density function of LDPE particle using PIV analysis: (a) horizontal velocity and (b) vertical velocity.

3.2.3 Effects of fluidization velocity and static bed height

In this section, the effects of both the gas velocity, U_f and static bed height, $H_{b0,}$ are investigated. For a 7.62 cm static bed height bed, the gas velocity is varied from 1.5 U_{mf} to 3 U_{mf}. The bed contains the same material including 149.3 g of LDPE particles and 100 wood pellets. For a 15.24 cm static bed height, the gas velocity is varied from 1.5 U_{mf} to 3.7 U_{mf}. The bed contains 298.6 g of LDPE particles and 100 wood pellets. Figure 3-17 shows the sample image for the 15.24 cm static bed height case. As expected, the expanded bed height increases with the increase of the fluidization velocity. At 1.5 U_{mf}, only LDPE particles are fluidized. The wood particles are well segregated from LDPE particles locating near the distributor plate (Figure 3-16a). Starting at 2 U_{mf}, both wood and LDPE particles are well mixed regardless of the gas velocity and the resulting expanded bed height. The general fluidization behavior for the 7.62 cm bed is similar (not shown).

To quantify the fluidization behavior for both cases, the mean and standard deviation of the total pressure drop, and the expanded bed height are provided in Figure 3-18 and Figure 3-19. The total pressure increases from 1.5U_{mf} to 2 U_{mf}, and start to drop after 2U_{mf}, for both static bed height (Figure 3-18). Additionally, increasing the static bed height causes both the mean and fluctuation of the total pressure drop signal. The bed height statistics generally follow similar trends. The mean bed height increases significantly from 1.5 - 2.0 U_{mf} transitioning from bubble bed to slug bed, and start to plateau after around 2 - 2.5 $U_{mf,}$ presumably due to the partial spout bed behavior discussed in section 3.1 – 3.2. (c.f. Figure 3.4)

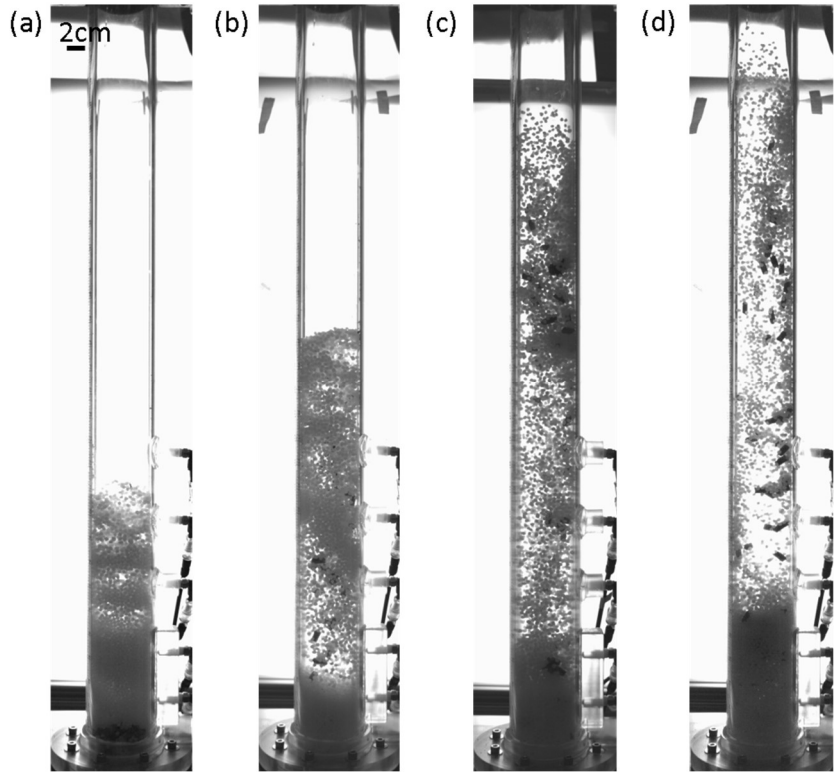

Figure 3-17: Sample image with varying fluidization velocity at 15.24 cm static bed height. (a) 1.5 U_{mf}, (b) 2 U_{mf}, (c) 2.5 U_{mf}, (d) 3 U_{mf}.

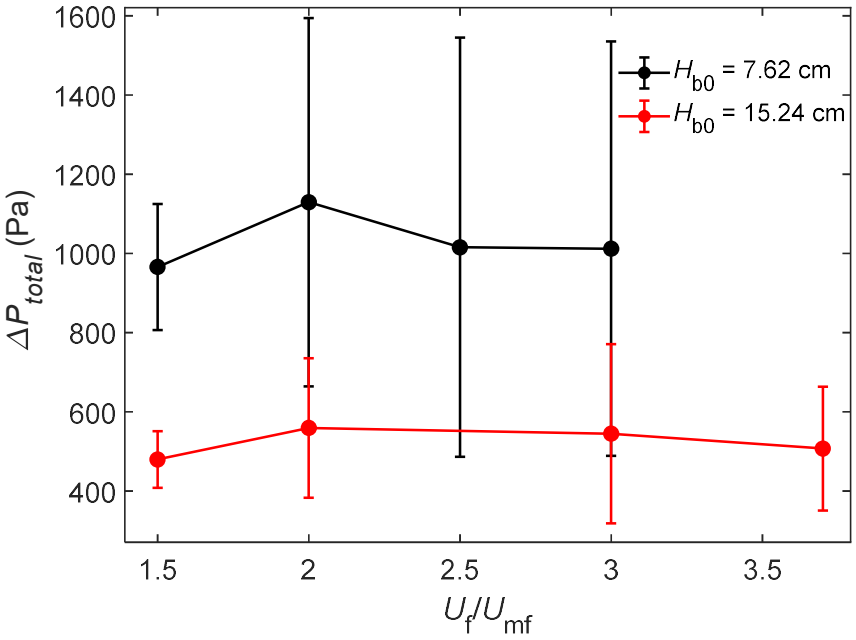

Figure 3-18: Effects of U_{mf} and static bed height on mean and fluctuation of pressure.

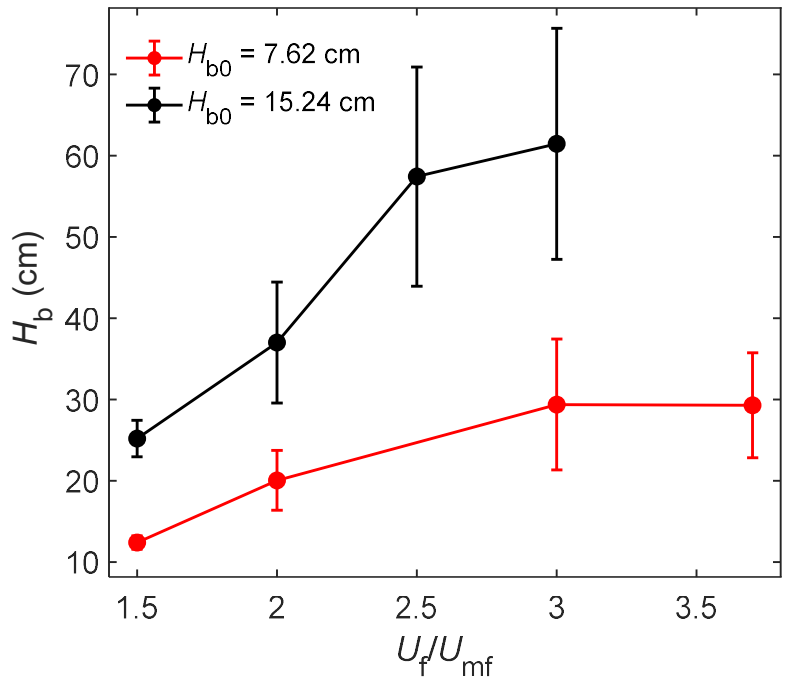

Figure 3-19: Effects of fluidization velocity and static bed height on mean and fluctuation of bed height.

3.3 BINARY FLUIDIZATION OF SAND AND WOOD PARTICLES

In this section, the statistics on the binary fluidization of Geldart B sand type and Geldart D type wood particles are summarized. The variables of interest include the biomass fraction, the static bed height, and the fluidization velocity.

3.3.1 Effects of biomass fraction

The effects of biomass fraction are investigated by varying the wood pellets fraction at 50 particles, 100 particles, and 200 particles. The corresponding particle masses are 21.7 g (0.434 g/particle), 42.6 – 42.9 g (0.426 -0.429 g/particle), and 85.1 g (0.426 g/particle). For all three cases, 729 g of sand particles are used in the bed, corresponding to a static bed height of 15.24 cm.

Sample images of the fluidization experiment at 4 U_{mf} are provided in Figure 3-20 with the AR=2 wood particle numbers ranging from 50 - 200. A complicated pattern of sand and wood particles mixtures is presented. It is technically challenging to distinguish between wood and sand particles. In the following analysis, we focus on the statistics of the bed height and pressure time series. The corresponding mean and standard deviation of the total pressure drop for 4 U_{mf} are shown in Figure 3-21. The power spectrum of the pressure signal is shown in Figure 3-22. As expected, with the increase number of wood particles, the total weight of the material also increases and thus the total pressure drops increases during fluidization. The standard deviation of the total pressure drops time series remains almost unchanged with varying wood pellets number in the bed. This is different from the binary fluidization of two Geldart D type particles as presented in section 3.2.2 (c.f. Figure 3-8). The detailed comparison for bi-fluidization of different types of particles pair is of interest for further investigation. The PSD peak frequency also remains unchanged at around 1.1 Hz for all three cases.

The bed height statistics are shown in Figure 3-23 and the corresponding PSD are shown in Figure 3-24. Similar to total pressure drop statistics, the mean bed height also increases with the increase of the number of wood pellets and the standard deviation of bed height signal also remains unchanged for three cases. Note, based on the high-speed imaging, the particles sometimes shoot over the acrylic section top into the HEPA filter and the maximum bed height for current measurement is only at the end of the acrylic section. As a result, all bed height measurements are impacted by the inherent cap effect and are all underestimated. The PSDs show a peak frequency around 1 Hz for 50 and 100 wood pellets case, whereas for 200 pellets case, the peak frequency is only at 0.53 Hz. The difference is possibly due to the capping effects from the bed height measurement. And the capping acts like a low-pass filter of the bed height signal, resulting in a lower frequency peak after conducting the fast Fourier transform.

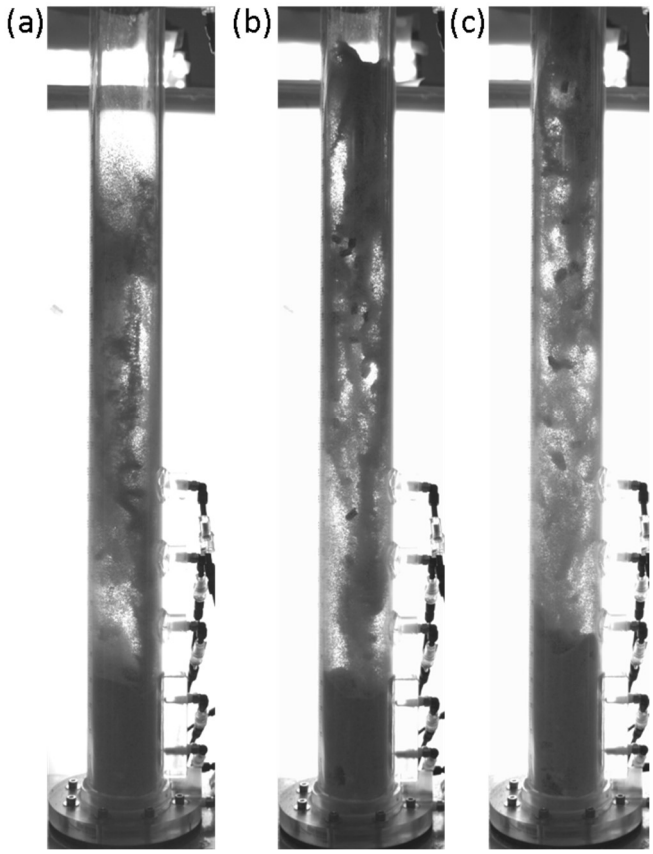

Figure 3-20: Sample image with varying biomass fraction at $4U_{mf}$ of sand particles. (a) 50 pellets, (b) 100 pellets, (c) 200 pellets.

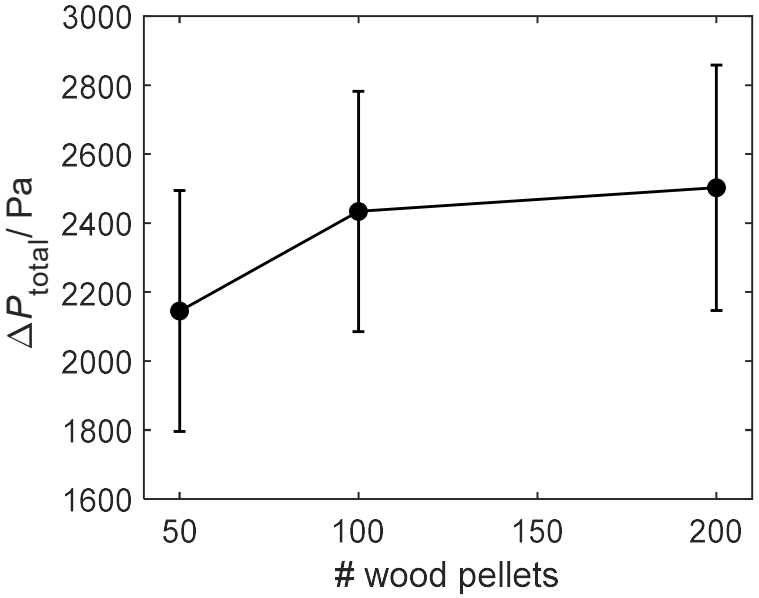

Figure 3-21: Mean and standard deviation of total pressure drop at 4 U_{mf} with varying number of wood pellets.

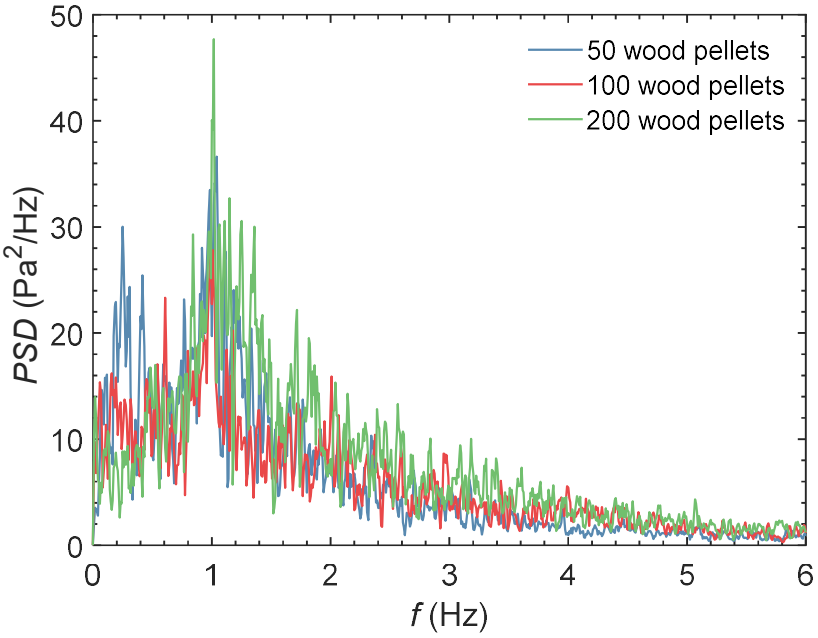

Figure 3-22: Effects of biomass fraction on the power spectrum density of the pressure signal at 4 U_{mf}.

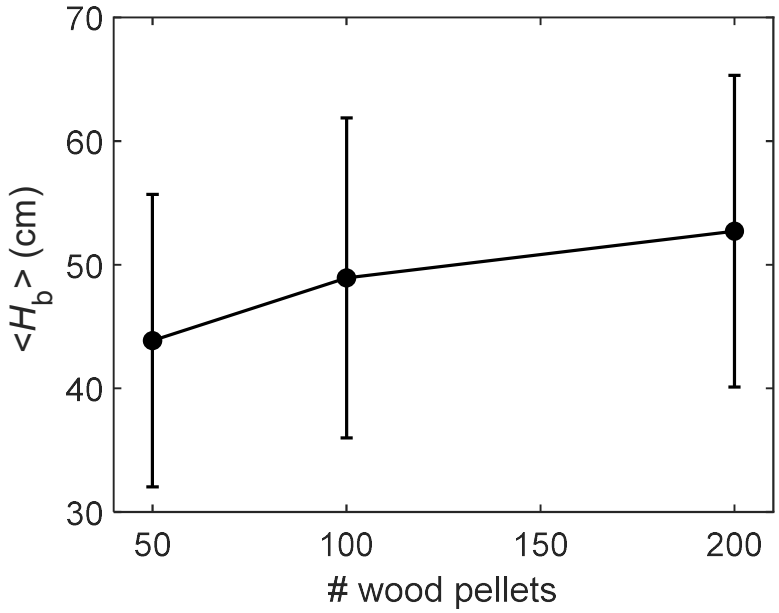

Figure 3-23: Mean and standard deviation of total pressure drop at 4 U_{mf} with varying number of wood pellets.

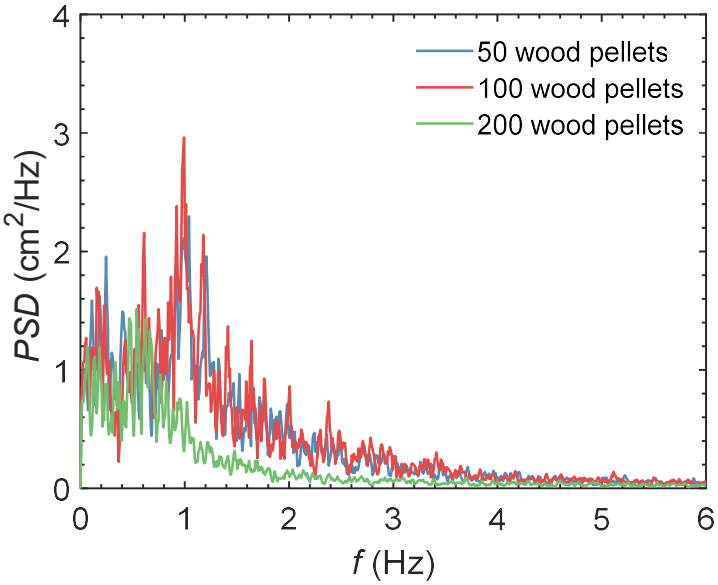

Figure 3-24: Effects of biomass fraction on power spectrum density of the bed height time series at 4 U_{mf}.

3.3.2 Effects of fluidization velocity and static bed height

In this section, the effects of both the gas velocity, U_f and static bed height, $H_{b0,}$ are investigated. For a 7.62 cm static bed height bed, the gas velocity is varied from 1.5 U_{mf} to 5 U_{mf}. The bed contains the same material including 364.5 g of sand particles and 100 wood pellets. For a 15.24 cm static bed height, the gas velocity is varied from 1.5 U_{mf} to 4 U_{mf}. The bed contains 729.0 g of sand and 100 wood pellets. Figure 3-25 provides the sample image for the 15.24cm static bed height case. As expected, the expanded bed height increases with the increase of the fluidization velocity. Different from LDPE/wood mixing case, wood particles are fluidized even at 1.5 U_{mf} of the sand and are often observed at the top of the bed. This is due to the density difference between sand and wood particles.

The total pressure drop signal characteristics are summarized in Figure 3-26 and 3-27. The mean total pressure increases with the increase of fluidization velocity and starts to plateau from 1.5 – 3 U_{mf} and even drops slightly for the shallower bed case from 3 U_{mf} to 5 U_{mf}. The standard deviation of the total pressure drop increases initially from 1.5 – 3 U_{mf}, and remains at the same level after 3 U_{mf} for both static bed height cases. Such behavior is presumably due to the transition from bubble bed to slug bed. For shallower and deeper beds, the standard deviation is similar at 1.5 Umf, however, the values for deeper beds becomes significantly larger than those for shallower bed after starting at 2 U_{mf}. For the corresponding power spectrum density (Figure 3-27), the peak frequency at 1.5 U_{mf} corresponding to the bubbling regime is the highest among all tested fluidization velocities with a value of 2.1 Hz for the shallower bed and 4.3 Hz for the deeper bed. The peak frequency decreases asymptotically with the increase of the fluidization velocity as the bed transitions from bubbling to slugging. The shallower bed has a peak frequency of 3.8 Hz, 3.1, Hz 2.6 Hz, and 2.4 Hz at 2 U_{mf}, 3 U_{mf}, 4 U_{mf}, and 5 U_{mf}, respectively. The deeper bed has a peak frequency of 1.9 Hz, 1.1 Hz, 1.0 Hz at 2 U_{mf}, 3 U_{mf}, and 4 U_{mf}, respectively. And the increase of the static bed height decreases the peak frequency for all tested fluidization velocities, as is also obvious from the figure.

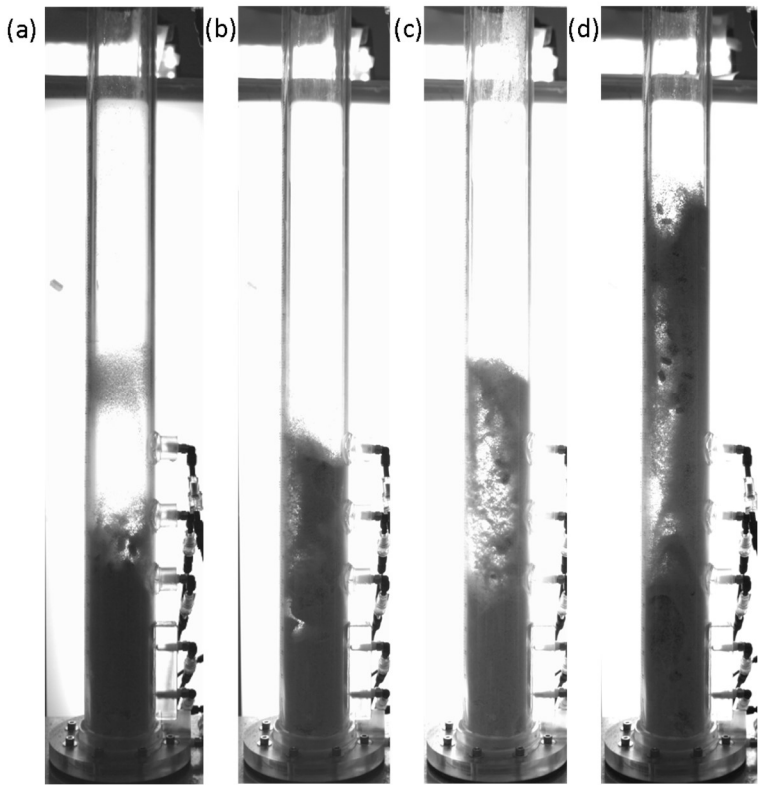

Figure 3-25: Sample image with varying fluidization velocity with a static bed height of 15.24 cm. (a) 1.5 U_{mf}, (b) 2.0 U_{mf}, (c) 3 U_{mf}, (d) 4 U_{mf}.

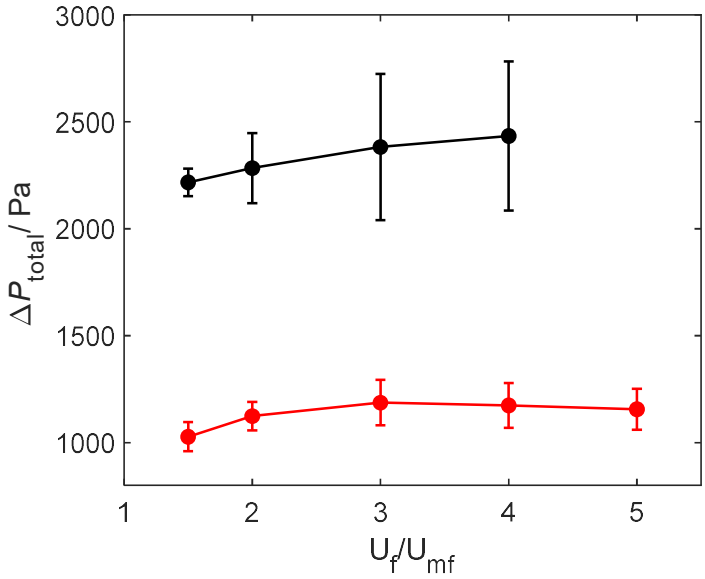

Figure 3-26: Mean and standard deviation of total pressure drop at varying fluidization velocity and two static bed heights (red: 7.62 cm, black: 15.24 cm).

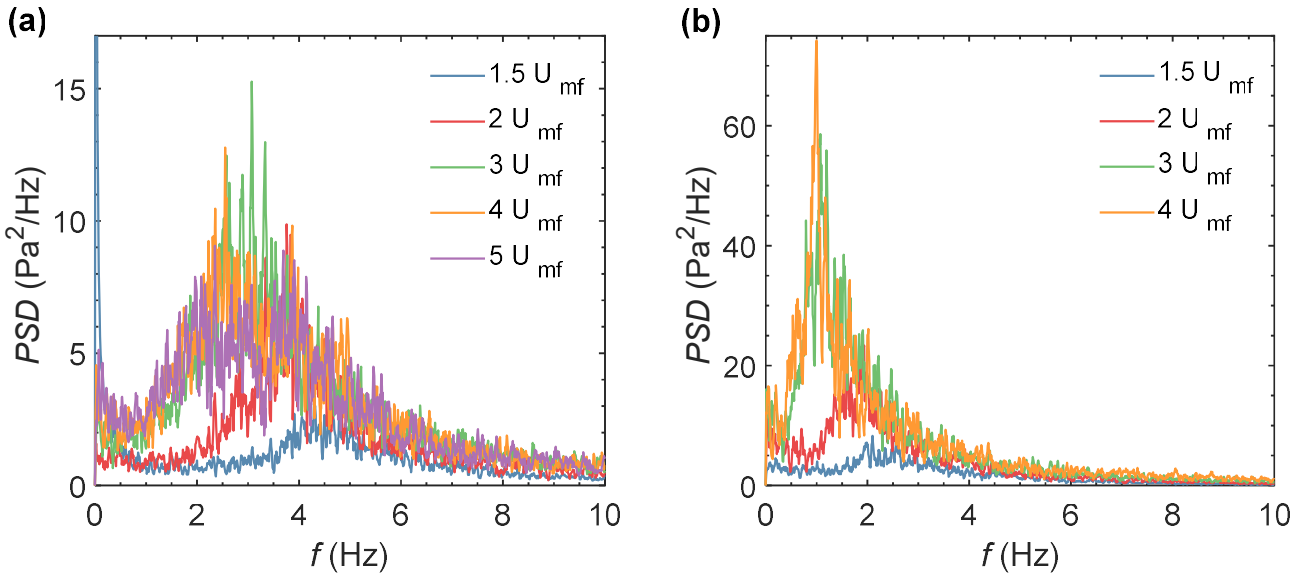

Figure 3-27: Comparison of the pressure power spectrum of varying fluidization velocities with a static bed height of (a) 7.62 cm and (b) 15.24 cm.

The mean and standard deviation of the bed height is shown in Figure 3-28. The mean bed height increases almost linearly with fluidization velocity for both bed height. The same trends also follow for the standard deviation. The increase of bed height increases both the mean and standard deviation of the bed height signals.

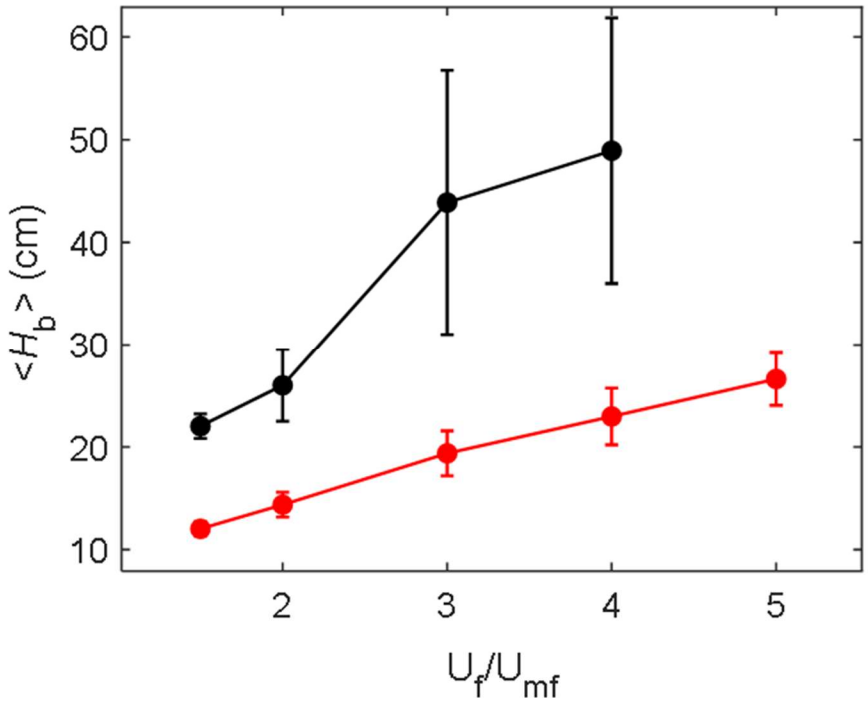

Figure 3-28: Mean and standard deviation of mean bed height at varying fluidization velocity and two static bed heights (red: 7.62 cm, black: 15.24 cm).

3.4 TERNARY FLUIDIZATION OF SAND, LDPE, AND WOOD PARTICLES

3.4.1 Effects of biomass fraction

For all runs in this section, 306.5 g of sand particles are used in the bed, corresponding to a static bed height of 7.62 cm. The effects of biomass fraction are investigated by varying the wood pellets fraction at 25 particles, 50 particles, and 100 particles. The corresponding particle masses are 10.7 g (0.428 g/particle), 21.4 g (0.428 g/particle), and 42.9 g (0.429 g/particle). The same amount of LDPE particle is also added, making the mass ratio between LDPE and wood particles 1:1.

Sample images of the ternary fluidization experiment with varying biomass fraction at 3 U_{mf} are provided in Figure 3-29. The corresponding mean and standard deviation of the total pressure drop are shown in Figure 3-30. The power spectrum density of the pressure signal is shown in Figure 3-31. As expected, with the increase number of wood particles, the total weight of the material also increases and thus the total pressure drop increases. The standard deviation of the total pressure drops time series remains almost unchanged with varying wood pellets number in the bed. The detailed comparison for bi-fluidization of different type of particles pair is of interest for further investigation. The shape of the PSDs is similar for all three cases with a slight decrease in peak frequency with the increase of biomass fraction. Similar trends can also be observed for the expanded bed mean/standard deviation as well as the PSD of the bed height (Figure 3-32, 3-33).

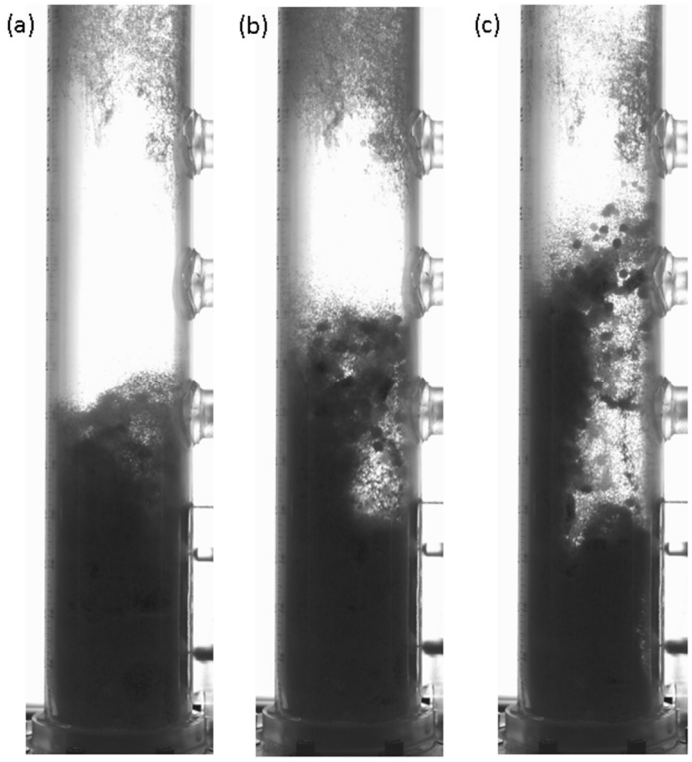

Figure 3-29: Sample image of ternary fluidization with varying biomass fraction at 3U_{mf} of sand particles. (a) 25 pellets, (b) 50 pellets, (c) 100 pellets.

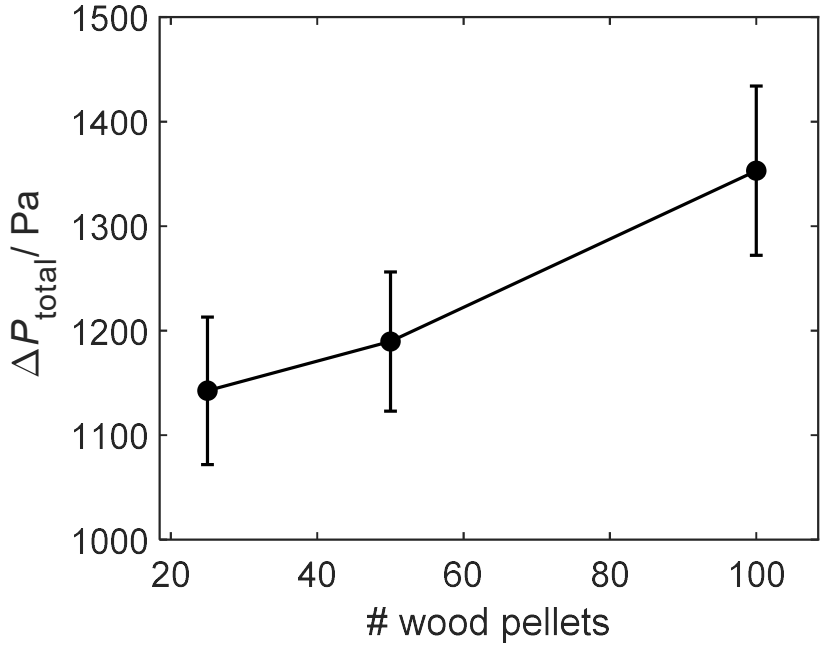

Figure 3-30: Mean and standard deviation of total pressure drop at 3 U_{mf} with varying number of wood pellets.

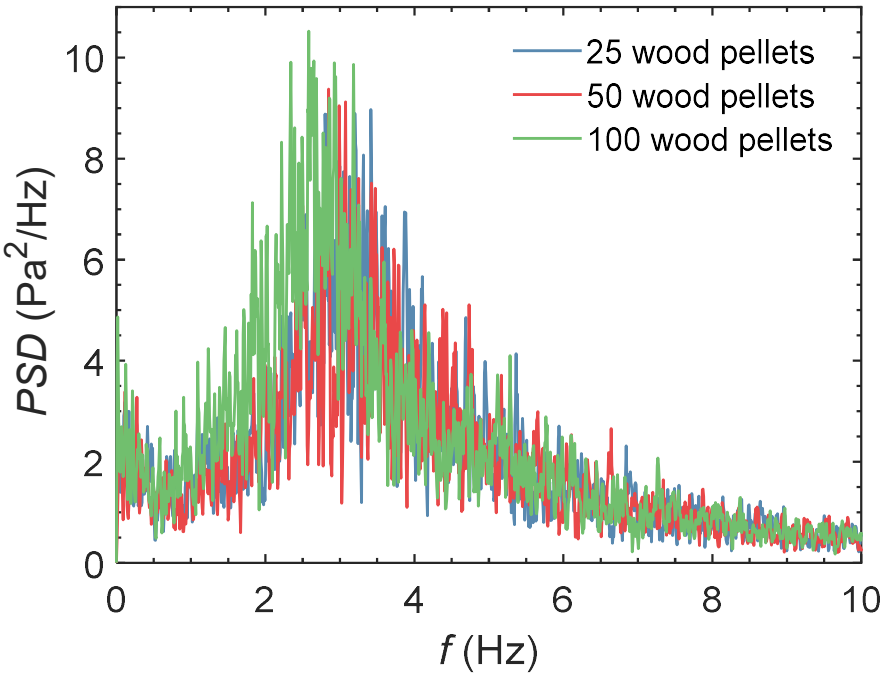

Figure 3-31: Effects of biomass fraction on power spectrum density of the pressure signal at 3 U_{mf}.

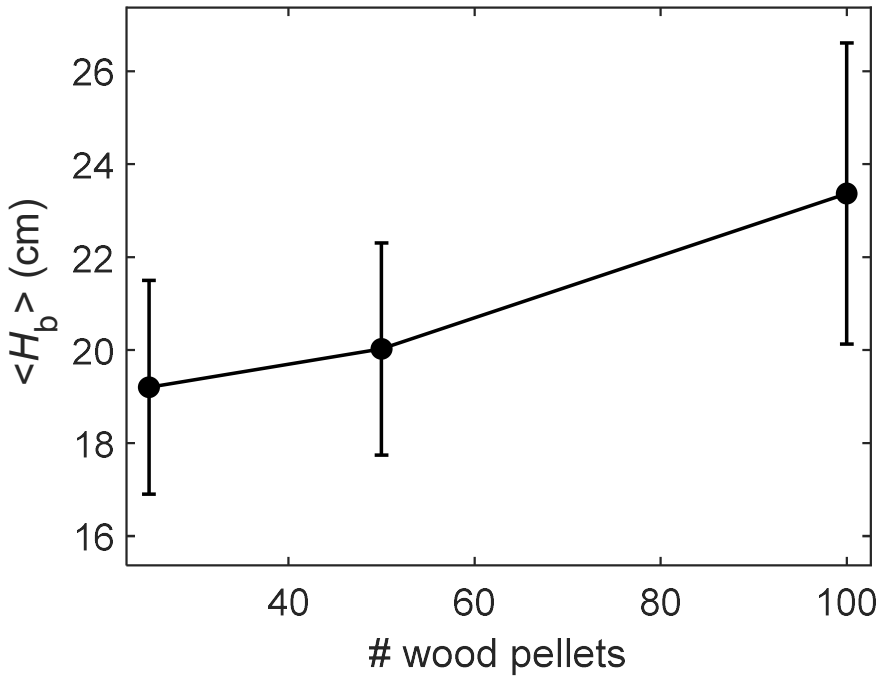

Figure 3-32: Mean and standard deviation of total pressure drop at 3 U_{mf} with varying number of wood pellets.

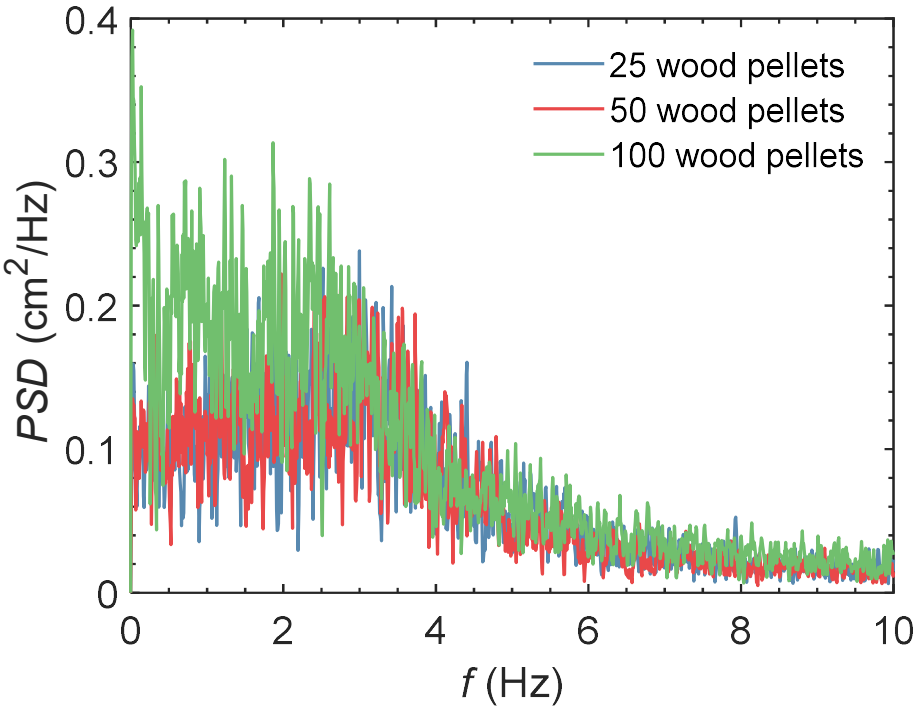

Figure 3-33: Mean and standard deviation of total pressure drop at 3 U_{mf} with varying number of wood pellets.

3.4.2 Effects of fluidization velocity

The fluidization velocity is varied from 1.5 Umf to 3 Umf to investigate the effects of fluidization velocity on the pressure and bed height signal. The bed material remains the same for all runs containing 306.5 g of sand particles, 21.4 g of LDPE particles, and 21.4 g of wood particles. The sand establishes a static bed height of 7.62 cm.

Sample images of the experiment at various fluidization velocities are provided in Figure 3-34. The mean and standard deviation of the total pressure is shown in Figure 3-35. The mean value increases initially from 1.5 – 2.0 U_{mf}, but drops slightly afterward, whereas the standard deviation increases with the increase of the fluidization velocity. The corresponding PSD shows a gradually decreasing peak frequency with the increase of the fluidization velocity (Figure 3-36). For the bed height statistics, the mean and standard deviation both increase almost linearly with the increase of the fluidization velocity (Figure 3-37). The PSD of the bed height time series peak frequency resembles the similar trends to the pressure signal, even though the peaks are not as sharp as those found in pressure signals, presumably due to the smearing effects that bed height identification during 2D imaging of the bed height.

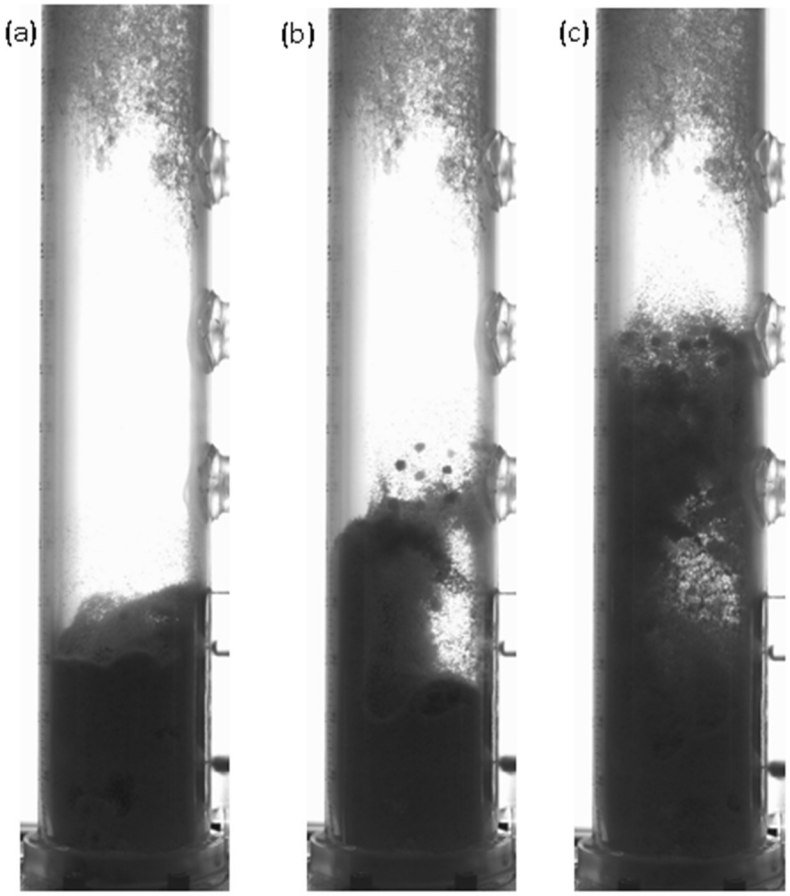

Figure 3-34: Sample image of ternary fluidization with varying fluidization velocity. (a) 1.5 U_{mf}, (b) 2.0 U_{mf}, (c) 3.0 U_{mf}.

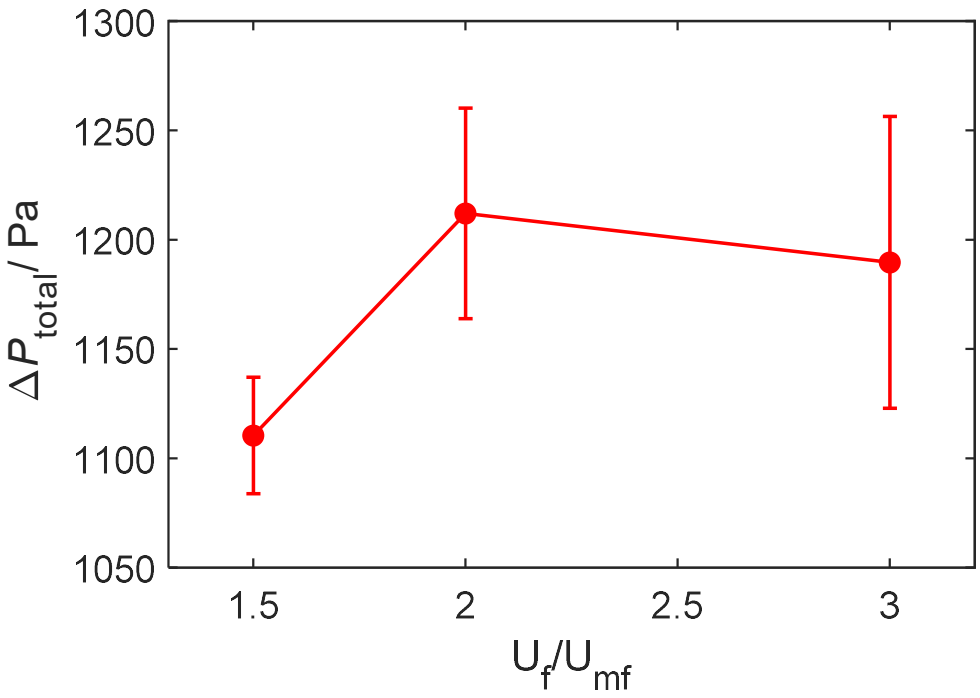

Figure 3-35: Mean and standard deviation of total pressure drop with varying fluidization velocity.

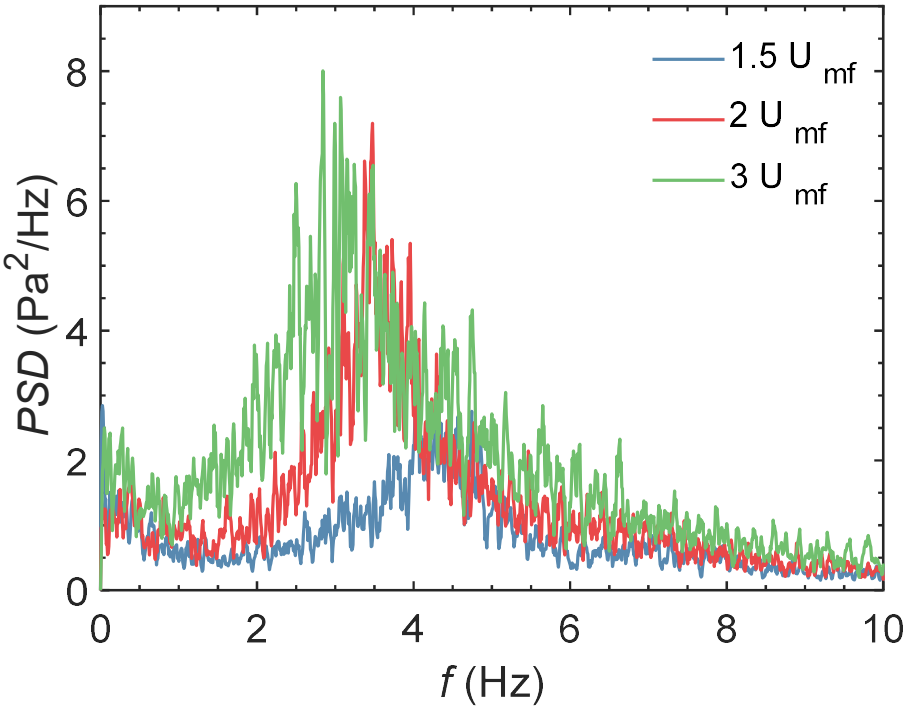

Figure 3-36: Effects of fluidization velocity on the power spectrum density of the pressure signal.

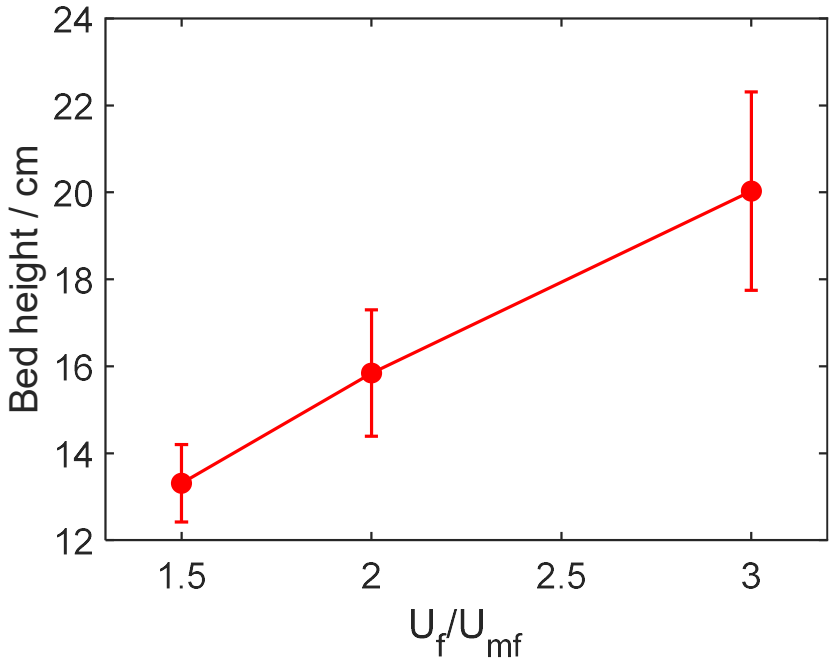

Figure 3-37: Mean and standard deviation of expanded bed height with varying fluidization velocity.

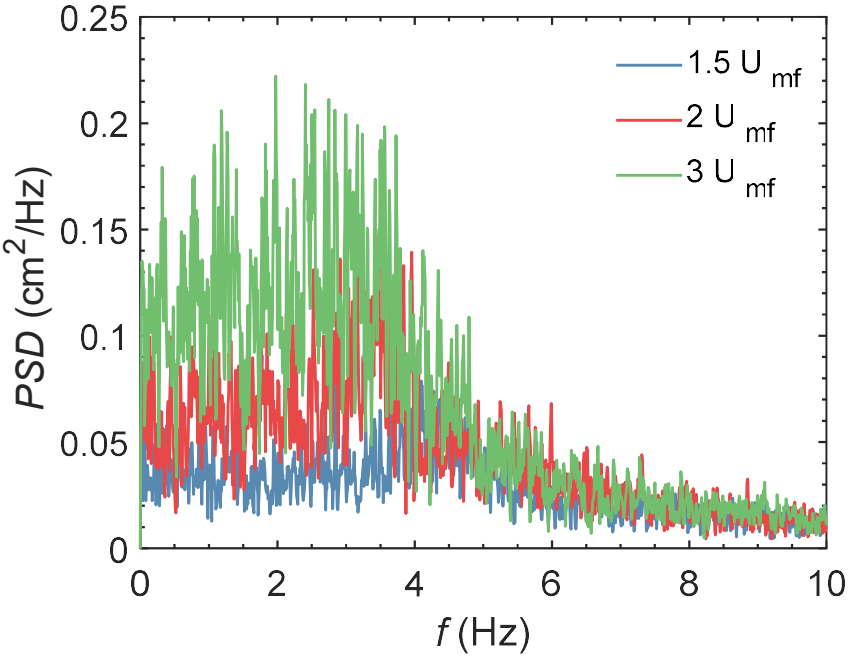

Figure 3-38: Effects of fluidization velocity on the power spectrum density of the pressure signal.

4. CONCLUSIONS

Detailed measurements have been made for various single, binary and ternary fluidization systems in a 2.5'' cylindrical bed made of acrylic with full optical access and multiple pressure ports at various height of the bed. The material of interests includes in the investigation include Geldart type D cylindrical hardwood pellets, Geldart type D spherical LDPE, and Geldart type B sand particles. The investigated parameters include biomass fraction, fluidization velocity and static bed height. Both high-speed imaging and pressure data have been acquired for analysis of the time-resolved bed height and pressure signal statistics. A machine learning algorithm has been used to segment different particle types in the high-speed recordings. The extracted particles are used to calculate the velocity of the particle field as well as the orientation of the non-spherical wood pellets.

Results of spherical LDPE particles show the bed presents a spouted bed behavior after around 3 U_{mf}, with a fountain region on the top of the bed, a slightly decreased mean bed height and significantly decreased bed height standard deviation. Before that, the bed transitions from bubbling at 1.4 U_{mf} to slugging at 2 U_{mf}.

For the binary fluidization of LDPE and wood particles, the standard deviation of the total pressure drops increase with the increase of the wood particle number at both 2.5 and 3.0 U_{mf}. The PSD peak frequency slightly decreases with the increase of biomass fraction at both fluidization velocities. The bed height statistics show that at 2.5 U_{mf}, the mean bed height increases with the increase of wood particles, however, at 3.0 U_{mf}, the mean bed height peaks at 100 wood particles and drops at 200 wood particles. The standard deviation of the bed height is similar for all cases, ranging from 11.4 - 14.2 cm without clear trends. The corresponding bed height power spectrum density resembles the pressure PSD in terms of orders of the peak frequencies. For all three cases, the orientation PDF all have a V-shape, with the dip in around 45°. The variation between runs seems to be minimal. The higher values of PDF at 0° is possibly due that the sampled particles tend to lie down when hitting the pool of LDPE particles, whereas particles tend to position vertically when bringing up by the air or falling. By varying fluidization velocities, the binary bed transitions from a bubble bed at 1.5 U_{mf} to a slug bed starting at 2 U_{mf}. The total pressure increases from 1.5U_{mf} to 2 U_{mf}, and start to drop after 2U_{mf}, for both static bed height. Additionally, increasing the static bed height causes both the mean and fluctuation of the total pressure drop signal. The mean bed height increases significantly from 1.5 - 2.0 U_{mf} transitioning from bubble bed to slug bed, and start to plateau after around 2 - 2.5 U_{mf}.

For the binary fluidization of sand and wood pellets, the total pressure drops increase with the increasing number of wood particles, while the standard deviation remains almost unchanged. The PSD peak frequency remains unchanged at around 1.1 Hz for all three cases. The mean bed height also increases with the increase of the number of wood pellets and the standard deviation of bed height signal also remains unchanged for all cases. By varying fluidization velocities, the mean total pressure drops increases with the increase of fluidization velocity and starts to plateau from 1.5 – 3 U_{mf} and even drops slightly for the shallower bed case from 3 U_{mf} to 5 U_{mf}. The peak frequency of the PSD decreases with the increase of the fluidization velocity at both tested static bed height. Additionally, the increase of static bed height decreases the peak frequencies in the PSD. The mean bed height increases almost linearly with fluidization velocity for both bed height. The same trends also follow for the standard deviation. The increase of the static bed height increases both the mean and standard deviation of the bed height signals.

For the ternary fluidization, the total pressure drop increases with the increase of wood particles, whereas the standard deviation remains unchanged. The increase of the wood pellets fraction causes the peak frequency identified in the pressure PSD to decrease slightly. The mean bed height shows similar trends. Increasing the fluidization velocity causes the mean and standard deviation of bed height to increase. The mean total pressure drops increase from 1.5- 2 U_{mf} but decrease slightly from 2-3 U_{mf}. The standard deviation increases with fluidization velocity. Both PSD of pressure and bed height show similar trends, namely, decreeing peak frequency with the increase of fluidization velocity.

Results from this systematic study provide several valuable datasets validating the computational models under various flow and particle conditions. Various types of simulations such as the Two-Fluid Model (TFM) based on the Eulerian approach and Lagrangian techniques such as Discrete Element Methods (DEM) can be applied to check their ability to the realization of related phenomena observed in the experiments. Furthermore, the detailed statistics on velocity, orientation, bed height, and pressure drop, needs to be compared to make sure the accuracy of the model.

5. REFERENCES

Abnisa F, Wan Daud WMA. 2014. A review on co-pyrolysis of biomass: An optional technique to obtain a high-grade pyrolysis oil. *Energy Convers. Manag.* 87:71–85

Araújo FHD, Silva RRV, Ushizima DM, Rezende MT, Carneiro CM, et al. 2019. Deep learning for cell image segmentation and ranking. *Comput. Med. Imaging Graph.* 72:13–21

Arganda-Carreras I, Kaynig V, Rueden C, Eliceiri KW, Schindelin J, et al. 2017. Trainable Weka Segmentation: A machine learning tool for microscopy pixel classification. *Bioinformatics*. 33(15):2424–26

Cocco R, Karri SBR, Knowlton T. 2014. Introduction to fluidization. *Chem. Eng. Prog.* 110(11):21–29

Costa P, Pinto F, Miranda M, André R, Rodrigues M. 2014. Study of the experimental conditions of the co-pyrolysis of rice husk and plastic wastes. *Chem. Eng. Trans.* 39(Special Issue):1639–44

Cui H, Grace JR. 2007. Fluidization of biomass particles: A review of experimental multiphase flow aspects. *Chem. Eng. Sci.* 62(1–2):45–55

Daghooghi M, Borazjani I. 2018. The effects of irregular shape on the particle stress of dilute suspensions. *J. Fluid Mech.* 839:663–92

Ferreira T, Rasband W. 2011. The ImageJ 1.44 User Guide

Gao X, Yu J, Li C, Panday R, Xu Y, et al. 2020. Comprehensive experimental investigation on biomass-glass beads binary fluidization: A data set for CFD model validation. *AIChE J.* 66(2):1–18

Geldart D. 1973. Elsevier Sequoia SA, Lausanne-Printed in the Netheriands Types of Gas Fhidization. *Powder Technol.* 7:285–92

Kunii D, Levenspiel O. 1991. *Fluidization Engineering*. Butterworth-Heinemann

Lormand C, Nemeth K, Palmer AS. 2018. Weka Trainable Segmentation Plugin in ImageJ: A Semi-Automatic Tool Applied to Crystal Size Distributions of Microlites in Volcanic Rocks

Martínez JD, Veses A, Mastral AM, Murillo R, Navarro M V., et al. 2014. Co-pyrolysis of biomass with waste tyres: Upgrading of liquid bio-fuel. *Fuel Process. Technol.* 119:263–71

Ouellette NT, Xu H, Bodenschatz E. 2006. A quantitative study of three-dimensional Lagrangian particle tracking algorithms. *Exp. Fluids*. 40(2):301–13

Pinto F, Franco C, André RN, Tavares C, Dias M, et al. 2003. Effect of experimental conditions on co-gasification of coal, biomass and plastics wastes with air/steam mixtures in a fluidized bed system. *Fuel*. 82(15–17):1967–76

Polan DF, Brady SL, Kaufman RA. 2016. Tissue segmentation of computed tomography images using a Random Forest algorithm: A feasibility study. *Phys. Med. Biol.* 61(17):6553–69

Thielicke W, Stamhuis EJ. 2014. PIVlab-time-resolved digital particle image velocimetry tool for MATLAB. *Publ. under BSD Licens. Program. with MATLAB*. 7(0.246):R14

Tucker JR, Shadle LJ, Benyahia S, Koepke ME, Mei J, Guenther C. 2013. Improvement in

precision, accuracy, and efficiency in standardizing the characterization of granular materials. *Proc. ASME 2013 Int. Mech. Eng. Congr. Expo.*, pp. 1–9

US Environmental Protection Agency. 2020. Advancing Sustainable Materials Management: 2018 Fact Sheet Assessing Trends in Materials Generation and Management in the United States. . (November):24

Xue Y, Zhou S, Brown RC, Kelkar A, Bai X. 2015. Fast pyrolysis of biomass and waste plastic in a fluidized bed reactor. *Fuel*. 156(September):40–46

Zhong W, Chen X, Zhang M. 2006. Hydrodynamic characteristics of spout-fluid bed: Pressure drop and minimum spouting/spout-fluidizing velocity. *Chem. Eng. J.* 118(1–2):37–46

Brian Anderson, Ph.D.
Director (Acting)
National Energy Technology Laboratory
U.S. Department of Energy

John Wimer
Associate Director
Strategic Planning
Science & Technology Strategic Plans
& Programs
National Energy Technology Laboratory
U.S. Department of Energy

Traci Rodosta
Strategic Planning
Science & Technology Strategic Plans
& Programs
National Energy Technology Laboratory
U.S. Department of Energy

Mark Ackiewicz
Director
Division of Carbon Capture and Storage
Office of Fossil Energy
U.S. Department of Energy

Bryan Morreale
Executive Director
Research & Innovation Center
National Energy Technology Laboratory
U.S. Department of Energy